

Spin-dimer ground state driven by consecutive charge and orbital ordering transitions in the anionic mixed-valence compound Rb_4O_6

T. Knaflič,¹ P. Jeglič,¹ M. Komelj,¹ A. Zorko,^{1,2} P. K. Biswas,³ A. N. Ponomaryov,⁴ S. A. Zvyagin,⁴ M. Reehuis,⁵ A. Hoser,⁵ M. Geiß,⁶ J. Janek,⁶ P. Adler,^{7,*} C. Felser,⁷ M. Jansen,^{7,†} and D. Arčon^{1,2,‡}

¹*Jožef Stefan Institute, Jamova c. 39, 1000 Ljubljana, Slovenia*

²*Faculty of Mathematics and Physics, University of Ljubljana, Jadranska c. 19, 1000 Ljubljana, Slovenia*

³*ISIS Pulsed Neutron and Muon Source, STFC Rutherford Appleton Laboratory, Didcot OX11 0QX, UK*

⁴*Dresden High Magnetic Field Laboratory (HLD-EMFL),*

Helmholtz-Zentrum Dresden-Rossendorf, 01328 Dresden, Germany

⁵*Helmholtz-Zentrum Berlin für Materialien und Energie, 14109 Berlin, Germany*

⁶*Institute of Physical Chemistry and Center for Materials Research,*

Justus-Liebig-University Giessen, Heinrich-Buff-Ring 17, 35392 Giessen, Germany

⁷*Max Planck Institute for Chemical Physics of Solids, Nöthnitzer Straße 40, 01187 Dresden, Germany*

(Dated: November 28, 2019)

Recently, a Verwey-type transition in the mixed-valence alkali sesquioxide Cs_4O_6 was deduced from the charge ordering of molecular peroxide O_2^{2-} and superoxide O_2^- anions accompanied by the structural transformation and a dramatic change in electronic conductivity [Adler et al, *Sci. Adv.* **4**, eaap7581 (2018)]. Here, we report that in the sister compound Rb_4O_6 a similar Verwey-type charge ordering transition is strongly linked to O_2^- orbital and spin dynamics. On cooling, a powder neutron diffraction experiment reveals a charge ordering and a cubic-to-tetragonal transition at $T_{\text{CO}} = 290$ K, which is followed by a further structural instability at $T_s = 92$ K that involves an additional reorientation of magnetic O_2^- anions. Magnetic resonance techniques supported by density functional theory computations suggest the emergence of a peculiar type of π^* -orbital ordering of the magnetically active O_2^- units, which promotes the formation of a quantum spin state composed of weakly coupled spin dimers. These results reveal that similarly as in $3d$ transition metal compounds, also in the π^* open-shell alkali sesquioxides the interplay between Jahn-Teller-like electron-lattice coupling and Kugel-Khomskii-type superexchange determines the nature of orbital ordering and the magnetic ground state.

I. INTRODUCTION

Research of mixed-valence compounds has come a long way over the course of roughly a century - from observing and explaining the interesting color in Prussian Blue [1], to studying charge ordering, giant magnetoresistance and superconductivity in various mixed-valence transition-metal compounds [2–4]. An interplay of lattice, charge, orbital and spin degrees of freedom is a common thread in these systems and one notable example of such phenomena is the Verwey transition in Fe_3O_4 [5]. In this archetypal mixed-valence compound comprising Fe^{2+} and Fe^{3+} ions at low temperatures, the structural transition characterized by charge ordering is accompanied by a significant drop in the sample conductivity and drastic change in the magnetic order. The Verwey transition is historically important, as it represents one of the first attempts to explain the metal to insulator transition in mixed-valence compounds [6]. However, the actual low-temperature charge ordering pattern, probably coupled to the structural fluctuations that persist well above the Verwey transition temperature, has recently turned out to be much more complex than originally anticipated

by Verwey [7, 8].

Alkali sesquioxides ($A_4\text{O}_6$, $A = \text{Rb}, \text{Cs}$) are anionic mixed-valence compounds with simple cubic structure at room temperature [Fig. 1(a)] and electronic states dominantly affected by π -molecular orbitals of O_2 units [9–13]. The four alkali metals donate four electrons to the three O_2 molecules, resulting in their average charge state of $\text{O}_2^{-4/3}$. Physically, three electrons are localized each on its own O_2 molecule, leaving the fourth one delocalized between structurally equivalent O_2 units. A structural transition from the cubic to the tetragonal phase [Fig. 1(b)] occurring in Cs_4O_6 at 250 K is accompanied by charge ordering [14, 15] as the fourth electron orders in such a way that a mixed-valence state of magnetic O_2^- and diamagnetic O_2^{2-} anions is formed in the ratio of 2:1. As a result, the conductivity drops by several orders of magnitude [14], bearing striking similarities with the Verwey transition [5]. The molecular nature of charge states allows charge dynamics to be followed by various spectroscopic techniques, such as Raman and impedance spectroscopy, showing that charge fluctuations happen in the cubic phase on a time scale of 10^{-12} s. Electron paramagnetic resonance (EPR) and nuclear magnetic resonance (NMR) techniques, on the other hand, demonstrate full charge localization in the tetragonal phase, on their time scales of 10^{-10} s and 10^{-6} s, respectively.

Obviously, the charge ordering in Cs_4O_6 has features in common with charge-ordering phenomena in transition

* adler@cpfs.mpg.de

† m.jansen@fkf.mpg.de

‡ denis.arcon@ijs.si

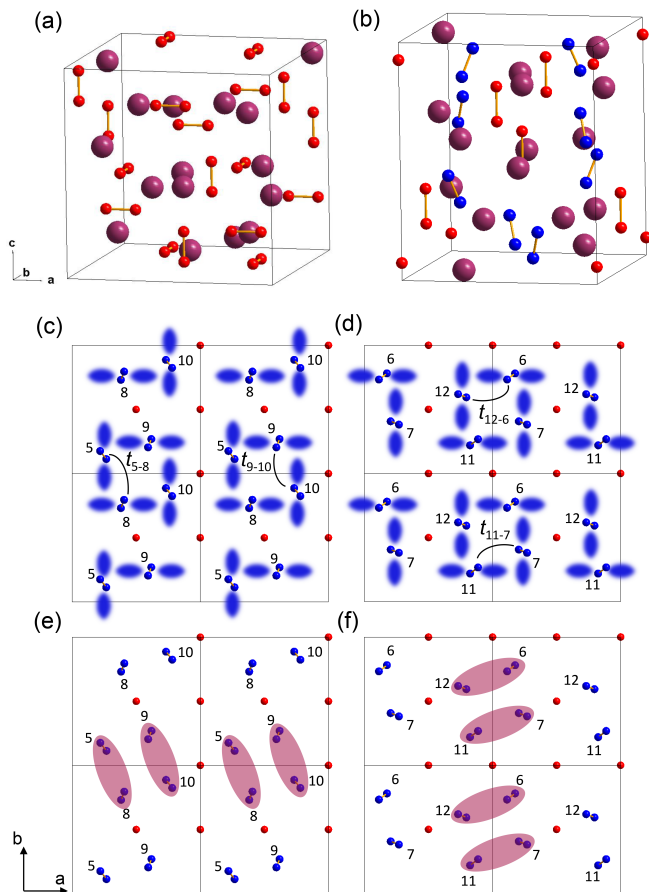


FIG. 1. Crystal structures of alkali sesquioxides A_4O_6 in (a) the high-temperature charge-disordered cubic (space group $I43d$) and (b) in the charge-ordered tetragonal (space group $I4$) phase. (c-d) The low-temperature tetragonal phase of Rb_4O_6 (space group $P4$) is characterized by an additional tilt of magnetic O_2^- units promoting their alternating π^* -orbital ordering (molecular orbital lobes of different O_2^- units labeled from 5 to 12 are indicated by the blue shaded areas). The structure is shown in the tetragonal $a-b$ plane for slices $0 \leq z \leq 0.5$ (c) and $0.5 \leq z \leq 1$ (d). Solid black lines in (c) and (d) show the main inter-site hopping integrals $t_{i,j}$ between nearest neighboring O_2^- i and j sites. The resulting formation of spin dimers depicted as pink ellipses are presented for $0 \leq z \leq 0.5$ (e) and for $0.5 \leq z \leq 1$ (f). In all figures, small blue spheres represent oxygen atoms in O_2^- units, small red spheres oxygen atoms in O_2^{2-} units and large violet spheres Rb atoms.

metal compounds like Fe_3O_4 or the manganites. In fact, analogies in the physical properties of the open p shell mixed-valence alkali sesquioxides as well as of the single-valence superoxides having merely magnetic O_2^- ions in their lattice with those of $3d$ transition metal compounds make them an attractive class of compounds for studying strongly correlated electron physics. Here, the lattice degree of freedom is determined by the tilting of the O_2^- units, which similarly as the Jahn-Teller effect in $3d$ systems, removes the degeneracy of the highest occupied π^* molecular orbitals and may give rise to orbital ordering.

For instance, in CsO_2 orbital ordering is suggested to drive the formation of quasi-one-dimensional spin chains [16–18], in analogy to $KCuF_3$ [19, 20], whereas RbO_2 does not show any signatures of low-dimensional magnetism [21]. The differences in the magnetic properties of the superoxides were attributed to differences in the low-temperature crystal structures leading to different tilting and thus orbital ordering patterns for the molecular O_2^- units [21, 22].

While the charge and lattice dynamics are now well understood in Cs_4O_6 , it remains unclear how the spin and orbital degrees of freedom in the mixed-valence sesquioxides respond to the Verwey-like charge ordering and whether similar structural and orbital fluctuations as in Fe_3O_4 exist and affect the low-temperature electronic state as well. Moreover, the nearly degenerate π^* strongly correlated states have to be treated explicitly in any realistic model where orbital degrees of freedom are included on equal footing with the electron spins, probably even involving Kugel-Khomskii-type superexchange [22–24]. Earlier theoretical calculations for A_4O_6 neglected such aspects and suggested a highly degenerate magnetic ground state, comprising of many competing noncollinear spin configurations [25]. In the present work we demonstrate that the magnetic properties of the sesquioxides A_4O_6 sensitively depend on the alkali cation A and that the differences in the magnetic properties can be traced back to the important coupling to π^* orbital degrees of freedom. We first show, that Rb_4O_6 at 290 K undergoes a Verwey-type charge-ordering transition from the cubic to a tetragonal structure of space group $I4$, which is the same as in Cs_4O_6 . In addition, however, Rb_4O_6 shows a further structural transition, which incorporates a peculiar type of π^* long-range orbital ordering below $T_s = 92$ K and promotes a strong antiferromagnetic coupling between pairs of O_2^- $S = 1/2$ spins. Thus, a magnetic ground state of weakly coupled spin dimers emerges in Rb_4O_6 within the charge and orbitally ordered state. Our results indicate that the orbital ordering in Rb_4O_6 at 92 K may be driven by exchange interactions (Kugel-Khomskii-type superexchange [23]) and demonstrate the strongly intertwined charge, orbital, spin and lattice degrees of freedom. These findings further extend the analogies between the physical phenomena of open-shell- p -electron systems and $3d$ compounds to mixed-valence alkali sesquioxides.

II. RESULTS

A. Charge ordering - Verwey transition

Powder neutron diffraction (PND) studies verify that Rb_4O_6 , similar as its sister compound Cs_4O_6 [14], undergoes a structural transition from the cubic (space group $I43d$, No. 220) to the tetragonal (space group $I4$, No. 82) crystal structure, which mainly proceeds between 290 and 250 K (Figs. S1 and S2 in Ref. [26]). Even when an

extremely slow cooling procedure is applied a fraction of 2.2% of cubic phase still persists at 2 K. The incomplete transformation reflects the kinetic hindrance of the transition, which involves a large reorientation of the molecular O_2 units. While in the cubic structure [Fig. 1(a)] the O_2 anions are oriented perpendicular to each other along the three equivalent crystal axes, in the tetragonal structure the diamagnetic O_2^{2-} align along the tetragonal c -axis whereas the two paramagnetic O_2^- ions per formula unit tilt by an angle β with respect to the c -axis. The large molecular reorientation, which is necessary to stabilize the tetragonal structure, gives rise to a first order structural transition with a thermal hysteresis width of ~ 100 K [Fig. 2 (a)] and most probably is also the main reason for the previously reported history dependence of the magneto-structural properties of the sesquioxides [13]. In fact, in a rapid quench-cooling experiment we are able to completely freeze-in the ambient-temperature cubic phase (Fig. S3 in Ref. [26]), which on warming remains metastable up to ~ 160 K, where it transforms into the more stable tetragonal phase (Fig. 2b). The tetragonal phase finally changes back into the high-temperature cubic phase in the temperature range between 350 and 370 K, irrespective of sample history.

Refinement of the high-resolution PND pattern collected at 400 K confirms the charge-disordered state of the cubic phase with peroxide and superoxide units occupying the same Wyckoff position in random distribution. The resulting O-O bond length amounts to 1.35 Å. Refinement of the 100 K PND pattern reveals distinct O_2^- and O_2^{2-} anions with O-O bond lengths of 1.31 and 1.52 Å, respectively, for the charge-ordered tetragonal structure (see Ref. [26] for refinement details). The O_2^- tilt angle $\beta \sim 20^\circ$ is slightly larger than $\beta \sim 17^\circ$ for Cs_4O_6 . The main difference to Cs_4O_6 is a smaller unit cell volume (788.4 Å³ and 920 Å³ for Rb_4O_6 and Cs_4O_6 , respectively) as the ionic radius of Rb^+ is smaller than that of Cs^+ , which has important implications for the structural and magnetic properties below 100 K as it will be described later.

The Verwey-type nature of the charge-ordering transition in Rb_4O_6 , just as for Cs_4O_6 [14], is apparent from a change in the electronic conductivity (see Ref. [26] for details of impedance spectroscopy measurements) by two orders of magnitude in response of the structural transition (Fig. 3). Local probe NMR and EPR techniques also detect freezing of the charge dynamics at the cubic to tetragonal transition on their respective time-scales. ^{87}Rb ($I = 3/2$) NMR measurements on a pristine sample in the cubic phase show no signal at room temperature [Fig. 4(a)]. This is reminiscent of Cs_4O_6 , where the absence of ^{133}Cs and ^{17}O NMR signals was attributed to strong relaxation effects in the cubic charge-disordered state [14]. Namely, as the charge rapidly fluctuates on the NMR time-scale of 10^{-6} s between equivalent O_2 units, both quadrupole and hyperfine coupling interactions are strongly modulated, thus reducing the nuclear relaxation times. On slow cooling, the ^{87}Rb NMR spec-

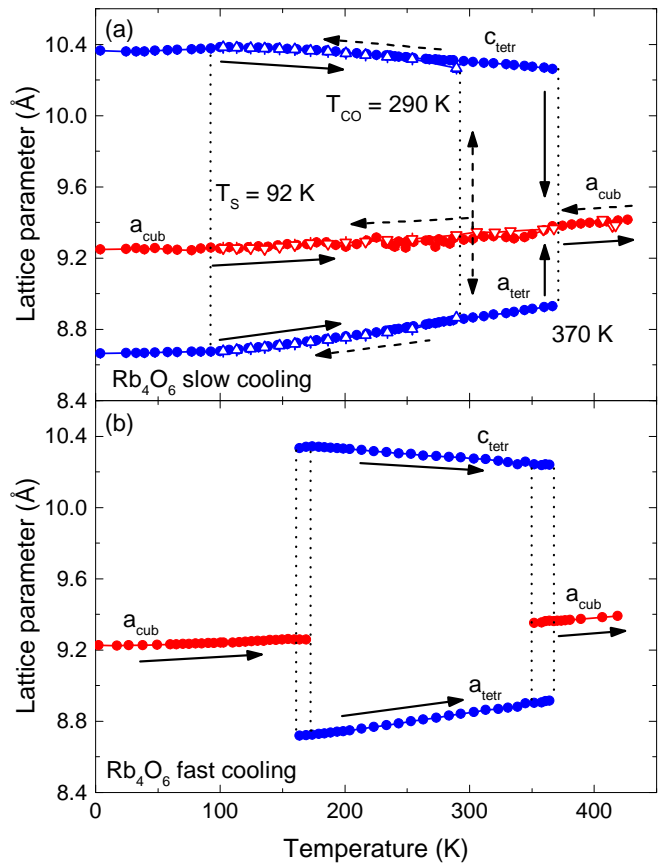


FIG. 2. The temperature dependencies of the lattice parameters for the cubic (red) and the tetragonal (blue) phases of Rb_4O_6 . (a) The temperature dependence of these parameters during the slow cooling (open triangles) and subsequent heating (circles) experiments. (b) Temperature dependencies of the lattice parameters for the measurements taken on warming after the quench-cooling thermal protocol. Dashed and solid arrows indicate cooling and heating temperature protocols respectively and the transformations from the cubic to the tetragonal and back to the cubic phases.

tra start to emerge below 250 K. This marks the suppression of ^{87}Rb relaxation rates due to the freezing of charge dynamics and the onset of charge ordering. Finally, in the X-band EPR measurements, the EPR signal appears on slow cooling as a very broad Lorentzian line below 250 K [Fig. 5(a) and Fig. S4]. The appearance of the EPR signal provides additional evidence for the cubic-tetragonal structural and charge-ordering transition on the EPR time-scale of 10^{-10} s. We note that in all these spectroscopic experiments, which are sensitive to the charge dynamics (i.e., impedance spectroscopy, EPR, and NMR), we find clear thermal hysteresis behavior [Figs. 3 and 4(a)] of the Verwey-like charge ordering transition.

Finally, in analogy to Cs_4O_6 [14], the structural/charge ordering phase transition in Rb_4O_6 is also reflected as a small anomaly in the molar magnetic susceptibility $\chi_m(T)$. This is particularly evident from the product

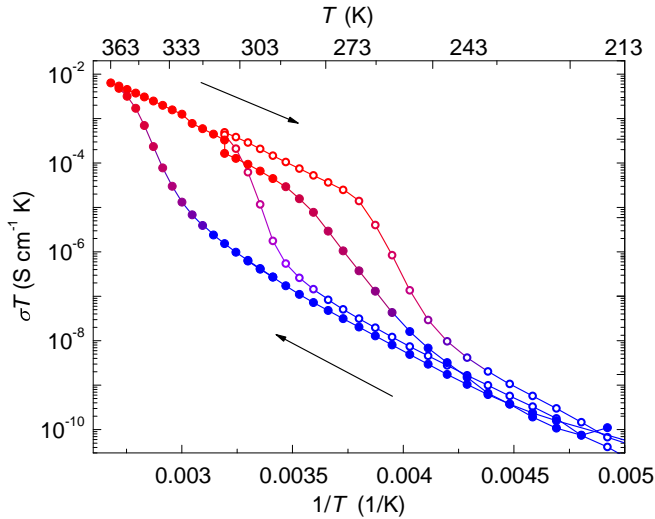


FIG. 3. Arrhenius plot of the conductivity σ multiplied by T for Rb_4O_6 (solid circles). For comparison, the data for Cs_4O_6 (open circles) [14] are shown. The color of symbols indicates the structure – red symbols stand for the cubic phase and blue symbols for the tetragonal phase.

$\chi_m T$, which suddenly decreases below 270 K on slow cooling from the initial $T = 400$ K and fully recovers back on warming at 375 K [inset to Fig. 5(d)].

B. The second structural transition - orbital ordering

A further structural phase transition is for Rb_4O_6 apparent from the emergence of additional Bragg reflections in the PND patterns collected at $T \leq 92$ K [Fig. 6(a) and (b)]. These reflections can be indexed as primitive reflections following the extinction rule $h + k + l = \text{odd}$, if persistence of a tetragonal unit cell is assumed. To demonstrate this, we compare in Fig. 6(a) the powder patterns collected at 3 and 107 K, where the presence of some prominent superstructure reflections is evident. The superstructure reflections appear at $T_s = 92$ K, as exemplified for the 311 reflection in Fig. 6(b). It is remarkable that the intensities of the reflections of the I -centered structure ($h + k + l = \text{even}$) remain practically unchanged. The violation of the extinction rule clearly indicates the loss of the I -centering and indeed, the high-resolution powder pattern of Rb_4O_6 collected at 3 K could be successfully refined in $P\bar{4}$ (space group No. 81), the maximal *klassengleiche* subgroup of $I\bar{4}$ (space group No. 82), see Fig. S2 and Tables S1 and S2 in Ref. [26] for the refinement results and calculated structural parameters.

The second structural transition at T_s is also reflected in an anomaly in the lattice parameters [Fig. 2 (a)]. While above 100 K a_{tet} decreases and c_{tet} increases with decreasing temperature, an inflection point in $a_{\text{tet}}(T)$ and a maximum in $c_{\text{tet}}(T)$ is seen near 100 K. In contrast to

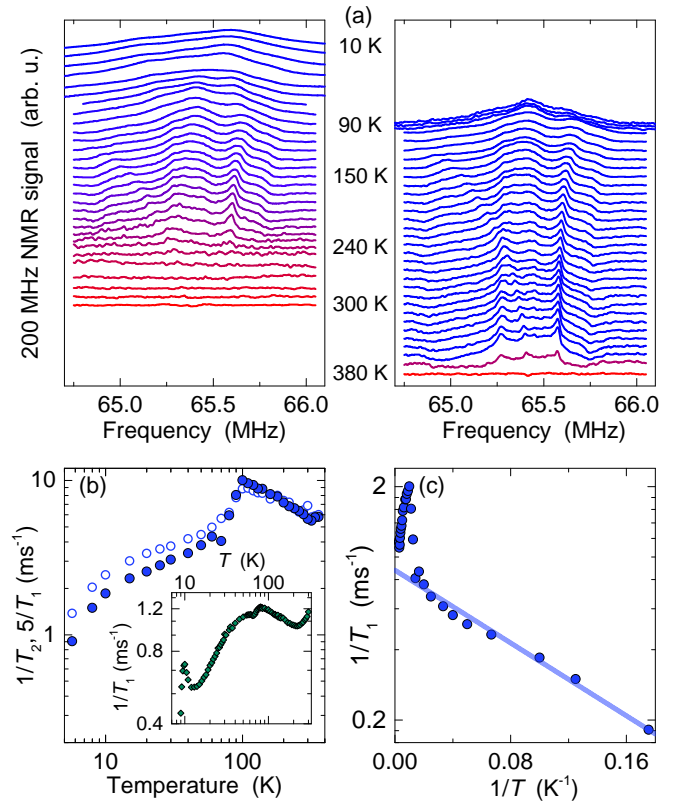


FIG. 4. (a) The temperature dependence of ^{87}Rb NMR spectra measured on cooling (left) and on heating (right). Red color of the spectra indicates the cubic phase while blue stands for the tetragonal phase. The horizontal base line for each spectrum indicate the temperature where it was measured. (b) The temperature dependencies of $5/T_1$ (solid circles) and $1/T_2$ (open circles) relaxation rates. In the inset, the ^{133}Cs $1/T_1$ data of CsO_2 is shown for comparison (data taken from [17]). (c) Solid circles show $1/T_1$ in the reciprocal $1/T$ scale. Linear regime of thermally activated behavior yielding a spin gap $\Delta_s/k_B = 9$ K is fitted for $T \leq 70$ K (solid line).

the cubic-tetragonal transition, the volume change of the $I\bar{4} - P\bar{4}$ transition ($\sim 5 \text{ \AA}^3$) is small and the thermal contraction is virtually isotropic. More importantly, as a consequence of the loss of the I -centering in course of the transition, in the low-temperature crystal structure the O atoms of the two O_2^- units are allowed to vary independently. One O_2^- dumbbell turns clockwise in the xy plane, whereas the other one turns anticlockwise (Table S2 in Ref. [26]). The averaged azimuth angle α for the two units of 40.2° is close to the value of 38.3° obtained at 100 K in the $I\bar{4}$ structure. Further, the tilting angles β against the c axis are similar for the two O_2^- units but somewhat larger than the value at 100 K, $\sim 20^\circ$ and $\sim 28^\circ$ respectively. These structural reorientations alter substantially the shortest intermolecular O-O distances. As displayed in Fig. 6(c) the shortest separations of the end oxygen atoms of superoxides form quadrilateral polygons in both polymorphs. In $I\bar{4}$ all edges are of the same lengths, the shorter ones among O3, the longer

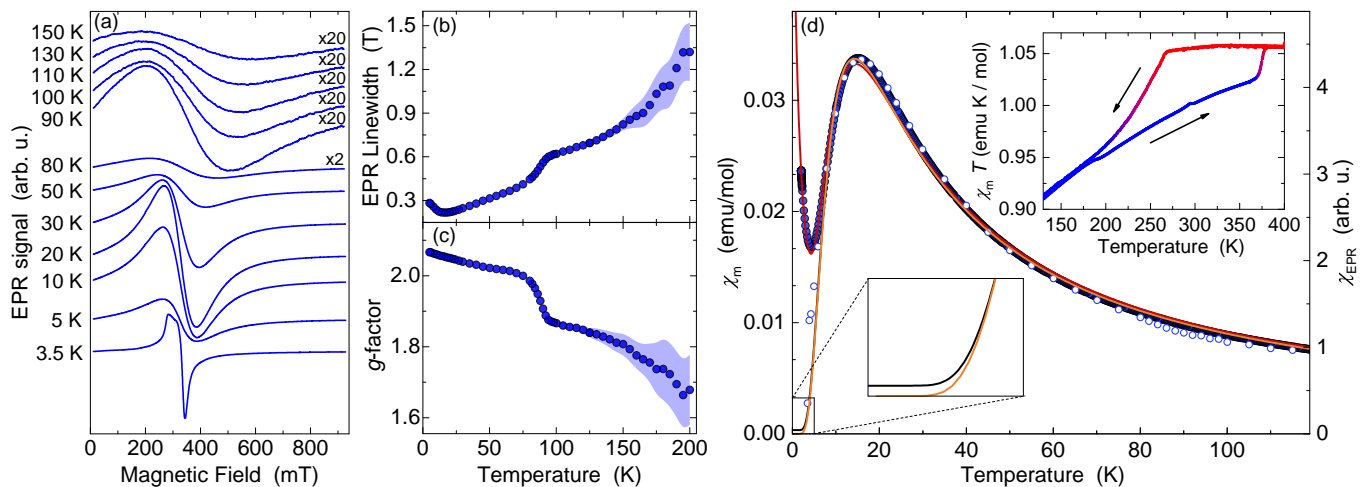


FIG. 5. (a) The temperature dependence of the X-band EPR signal. (b) The temperature dependence of EPR linewidth and (c) of g -factor. The blue area at high temperatures indicates the level of uncertainty. (d) The temperature dependence of the molar spin susceptibility as obtained from bulk magnetization (solid circles) and EPR (open circles) measurements. The red line shows an isolated-dimer-model (Eq. 1) fit to the magnetic susceptibility data with an added small paramagnetic contribution. The orange line is an isolated-dimer-model fit to EPR data with no paramagnetic contribution. The black line shows a small correction to the spin susceptibility for the added DM interaction of 2.5 K (expanded low-temperature range is shown in the small inset). The inset presents the $\chi_m T$ data revealing anomalies associated with the cubic-tetragonal and the reverse tetragonal-cubic transition.

ones among O4. In $P\bar{4}$ this situation is changed, and moreover, the shorter bond lengths are splitting into two slightly different lengths, which again reflects symmetry breaking. As the active π^* molecular orbitals have their lobes oriented perpendicular to the O-O bond axis, the structural transition at T_s should lead to a change in the orbital ordering pattern and affect the exchange interaction pathways.

The structural $I\bar{4} - P\bar{4}$ transition at T_s is dramatically reflected in the magnetic properties probed by local probes of NMR and EPR. In the high-temperature tetragonal phase, the ^{87}Rb NMR spectra have a characteristic quadrupolar powder lineshape with singularities of the central $-1/2 \leftrightarrow 1/2$ transition, split by ~ 300 kHz. As the temperature is lowered, the spectra further broaden and the singularities become less pronounced. At around T_s , there is a change in the ^{87}Rb NMR lineshape. The quadrupolar singularities are no longer visible and the spectrum below T_s begins to adopt the shape of a very broad, almost featureless resonance.

The low-temperature broadening of the ^{87}Rb NMR resonance suggests a change in the hyperfine coupling fields, whereas the accompanying disappearance of the quadrupole singularities is consistent with a structural distortion that affects the ^{87}Rb quadrupole interaction via the electric field gradient. In order to throw some additional light on the transition at T_s , we next turn to ^{87}Rb spin-lattice and spin-spin relaxation measurements. In the high-temperature tetragonal phase, $1/T_1$ at first increases with decreasing temperature [Fig. 4(b)]. The spin-lattice relaxation rate is suddenly suppressed at T_s by a factor of ~ 2 within a 20 K interval and then

it monotonically decreases with decreasing temperatures down to 5 K. $1/T_2$ has, within a factor of 5 in magnitude, an identical temperature dependence as $1/T_1$. This implies that both relaxation rates are governed by the same local-field fluctuations of purely magnetic origin with very short correlation times that dramatically change at T_s .

Remarkably, the temperature dependence of the ^{87}Rb $1/T_1$ in Rb_4O_6 is qualitatively very similar to that of the ^{133}Cs $1/T_1$ in CsO_2 [inset in Fig. 4(b) and Ref. [17]]. In CsO_2 , the increase of $1/T_1$ with decreasing temperature between 220 and 80 K was ascribed to the dynamic modulation of the antiferromagnetic exchange coupling between nearest-neighbouring O_2^- spins due to their thermal librations [17]. O_2^- librations at ~ 80 K suddenly freeze-out and trigger the structural transition from the tetragonal to the orthorhombic phase [16]. In the orthorhombic phase the O_2^- dumbbells tilt and, as a result, the double degeneracy of O_2^- molecular orbitals is lifted, thereby allowing orbital ordering that promotes the formation of antiferromagnetic spin chains to establish. The resemblance of ^{87}Rb $1/T_1$ in Rb_4O_6 to that of CsO_2 for temperatures above and around T_s leads us to the suggestion that similar librations of O_2 units in the tetragonal phase also determine the ^{87}Rb $1/T_1$ for $T > T_s$, while the freeze-out of the O_2 librations at the structural transition at T_s is accompanied by a concomitant change in the oxygen dumbbell π^* orbital order.

Plotting $1/T_1$ in logarithmic scale versus $1/T$ shows a straight line for $T \leq 70$ K [Fig. 4(c)]. Such thermally activated behavior of $1/T_1$ (and also of $1/T_2$) demonstrates the opening of a spin gap in the spectrum of low-energy

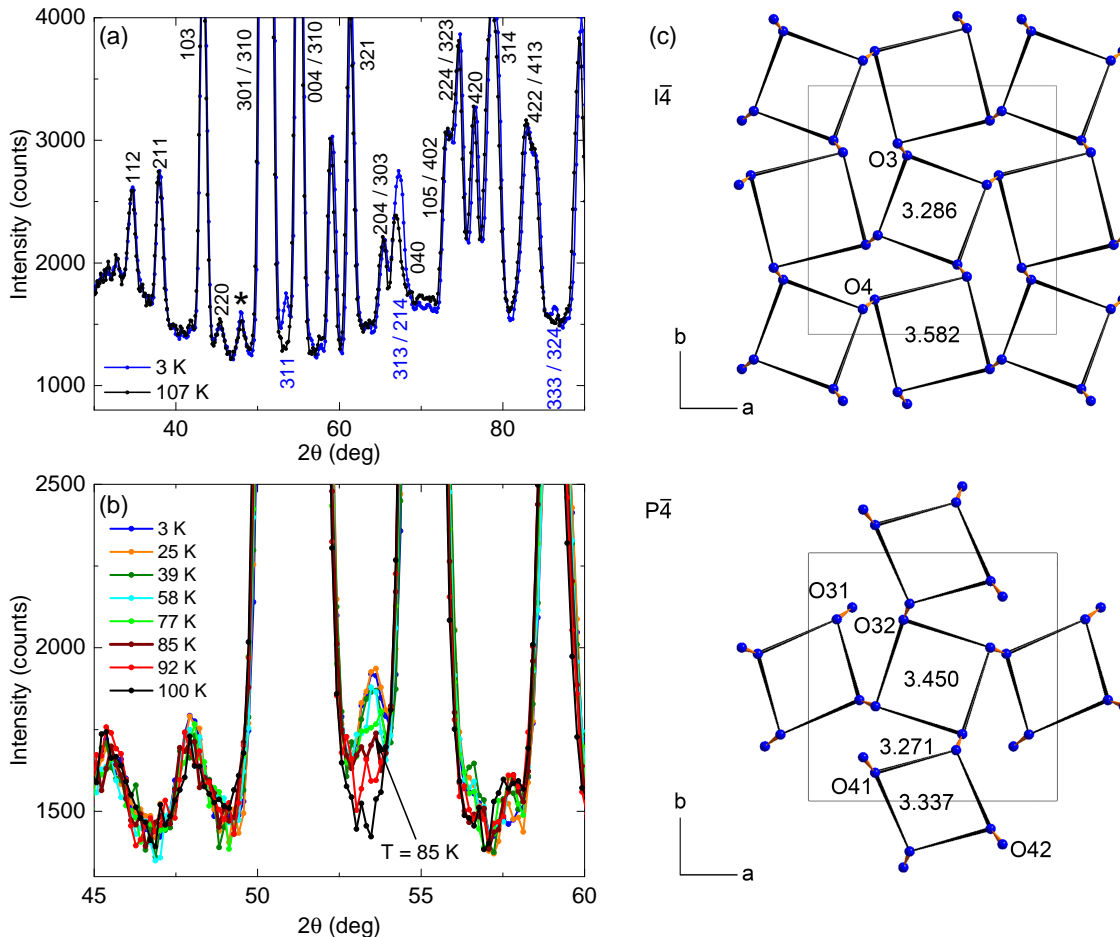


FIG. 6. (a) Powder neutron patterns of Rb_4O_6 collected on the instrument E6 ($\lambda = 2.426 \text{ \AA}$) at 3 and 107 K. At 3 K additional weak reflections have been detected, which can be indexed as primitive reflections following the extinction rule $h + k + l = \text{odd}$ (labeled in blue) and which are forbidden in the I -centered tetragonal structure obeying the rule $h + k + l = \text{even}$ (labeled in black). The asterisk indicates the main reflection of residual cubic phase. (b) Powder neutron patterns in a reduced 2θ range showing the temperature dependence of the superstructure reflection 311. (c) Shortest intermolecular oxygen separations in the high-temperature $I\bar{4}$ (top) and the low-temperature $P\bar{4}$ (bottom) structure of Rb_4O_6 . Atomic labels are as in Table S2 (the equivalent molecule labels as used in Fig. 1 are given in Table S3), distances are in \AA . In $I\bar{4}$ all quadrilateral polygons are formed by symmetry equivalent oxygen atoms resulting in degenerate lengths of the edges and in a point group symmetry of $\bar{4}$ for both sets of polygons. In $P\bar{4}$ the coupling of the original O4 atoms due to space group symmetry is removed and the degeneracy of the intermolecular separations of O41 and O42 is lifted, while the sub-sets of O31 and O32 still form equilateral polygons of local 4 symmetry, although of substantially different lengths.

spin excitations. By fitting the $1/T_1$ data below 70 K to $1/T_1 = A \exp(-\Delta_s/k_B T)$ we extract the size of the spin gap $\Delta_s/k_B = 9 \text{ K}$ in the magnetic field of 9.39 T. We note that no evidence for the opening of a spin gap at low temperatures has been observed in $1/T_1$ data taken on the sister compound Cs_4O_6 [13], which suggests a fundamental difference in their magnetic ground states. It is also fundamentally different from CsO_2 , where the orbital ordering leads to the formation of the antiferromagnetic chains of O_2^- $S = 1/2$ moments with the gapless Tomonaga-Luttinger-liquid state [17, 18]. The presence of a spin gap in the excitation spectrum of Rb_4O_6 thus infers a new kind of low-temperature orbital order, which favors the antiferromagnetic coupling between pairs of

O_2^- spins.

In agreement with the NMR and structural data, we find a clear anomaly at T_s in the X-band EPR linewidth and in the g -factor [Fig. 5(b) and (c)]. The latter is particularly dramatic, as the g -factor increases from 1.8714 to the low-temperature value of 1.9997 in a narrow temperature interval of about 15 K. The components of the g -factor tensor explicitly depend on the splitting between π^* orbitals [13, 27], so the change in the g -factor at T_s is consistent with the structural $I\bar{4} - P\bar{4}$ transition where the tilting of O_2^- units changes. Moreover, if the low-temperature orbital order indeed affects the exchange coupling between the nearest neighboring O_2^- groups, then also the EPR linewidth, which is in the exchange-

narrowing limit given by $\Delta B \approx M_2/J$ [28] (here M_2 is the second moment of the magnetic anisotropic interactions), is expected to change too. Therefore, the narrowing of the EPR signal from $\Delta B = 600$ mT at 95 K to $\Delta B = 450$ mT at 80 K is yet another evidence of the correlation between structural and orbital order on one side and the spin state emerging from the modification of exchange coupling constants at T_s on the other.

C. Coupling of the magnetic properties to the orbital order below T_s

Below T_s , the molar magnetic susceptibility $\chi_m(T)$ of Rb_4O_6 monotonically increases with decreasing temperature [Fig. 5(d)] and shows a pronounced maximum at $T_{\text{max}} = 15$ K, below which it is rapidly suppressed. At the lowest temperatures, a Curie upturn dominates $\chi_m(T)$, which can be attributed to unpaired O_2^- ions due to the residual charge and orbitally disordered cubic phase of Rb_4O_6 . This is corroborated by an increased Curie tail observed after the more rapid cooling down to 2 K, where a larger fraction of the cubic phase is frozen-in (Fig. S5 in Ref. [26]).

The integrated X-band EPR signal intensity, $\chi_{\text{EPR}}(T)$ closely mimics $\chi_m(T)$, i.e., it shows a pronounced maximum at T_{max} , below which the EPR signal rapidly disappears due to the existence of a spin gap [Fig. 5(d)]. At the lowest temperatures, only a significantly narrower signal with a small axially-symmetric g -factor anisotropy ($g_{\perp} = 1.9757$ and $g_{\parallel} = 2.311$) is observed [Fig. 5(a) and Fig. S6 in Ref. [26] for the lineshape fit]. In a control X-band EPR experiment using a quench cooling protocol from 400 K, we measured the EPR signal of the quenched cubic phase alone (Fig. S7 in Ref. [26]). This signal, whose intensity nicely follows the Curie-like temperature dependence (Fig. S8 in Ref. [26]), is by a factor of ~ 100 broader than the g -factor broadened low-temperature signal in the slow-cooling experiments and thus cannot explain the peculiar X-band EPR residual response at low temperatures. Alternatively, the origin of the unpaired O_2^- moments that contribute to such signal may be due to some structural fluctuations with the fourth charge localizing on the "wrong" O_2 unit or even its delocalisation over several O_2 units around such defect. A possible realization of such structural fluctuation would be a defect that includes O_2 unit, which has not flipped from its original cubic orientation during the cubic-to-tetragonal transition. In this respect, the presence of structural fluctuations deep in the Verwey charge ordered phase may be reminiscent of "trimerons" in the canonical Verwey system Fe_3O_4 [7].

We note that neither the low-temperature maximum in $\chi_m(T)$ nor the anomalies at higher temperatures were apparent in earlier studies of the magnetic properties of Rb_4O_6 [29]. As in the time of these studies the structural transitions were still unknown, possibly quite rapid cooling procedures were applied and thus rather the cu-

bic or mixtures of the cubic and tetragonal phase were investigated at low temperatures. This rationalizes also the irreversibility in the $\chi_m(T)$ curves which was previously attributed to frustration effects [29] and underpins the crucial role played by the orbital order for the low-temperature spin state.

In contrast to the pure superoxides CsO_2 and RbO_2 in which O_2^- spins ultimately undergo three-dimensional antiferromagnetic order near 10 K [17, 18] and 15 K [21], respectively, there are no indications for long-range magnetic order from the neutron diffraction patterns of the Cs_4O_6 [14, 15] and Rb_4O_6 [Fig. 6(a)]. The absence of long-range magnetic order in Rb_4O_6 is here unambiguously confirmed by muon spin relaxation (μSR) experiments down to 1.6 K. The μSR asymmetry $A(t)$ measured at $T = 1.6$ K in an applied transverse field (TF) of $B_{\text{TF}} = 2.0$ mT oscillates with the expected full initial asymmetry $A_0 = 0.238$ and frequency $\nu = 273.6$ kHz. This frequency corresponds well to the applied field ($\nu_{\text{TF}} = \gamma_{\mu} B_{\text{TF}}/2\pi$, here $\gamma_{\mu} = 2\pi \cdot 135.5$ MHz/T is the muon gyromagnetic ratio), ruling out the presence of any ordered static internal fields. The absence of static internal fields is also revealed in zero-field (ZF) measurements, where the μSR asymmetry exhibits a stretched-exponential type of decay [Fig. 7(a)] due to the fluctuating O_2^- spins in the vicinity of the muon stopping site. Most importantly, we find no oscillations in $A(t)$ that would suggest long-range magnetic order. Moreover, the absence of a Kubo-Toyabe-like dip [30] in $A(t)$ up to 15 μs limits any disordered static local fields at the muon stopping sites to values below ~ 0.1 mT and thus corroborates a dynamic nature of the O_2^- spins even at the lowest temperatures. The lack of any static magnetic order in the alkali sesquioxides is an important difference to the canonical Verwey system Fe_3O_4 .

The low-temperature $\chi_m(T)$ of Rb_4O_6 is in striking contrast to that of Cs_4O_6 , for which a Curie-Weiss-like $\chi_m(T)$ was reported down to 2 K [14]. This must originate from the difference in the orbital order as the second structural transition at T_s is absent in Cs_4O_6 . The broad maximum in $\chi_m(T)$ and an activated type behavior of $1/T_1$ are signatures of a gapped low-dimensional magnetism in Rb_4O_6 . The simplest model that explains these findings is that of isolated dimers forming a singlet ground state. In this case, the molar magnetic susceptibility is given by the Bleaney-Bowers (BB) expression [31]

$$\chi_m(T) = \frac{8C_{1/2}}{T(3 + \exp(J/k_B T))}. \quad (1)$$

Here, J is the intra-dimer exchange coupling constant and $C_{1/2} = N_A \mu_0 \mu_B^2 g^2 / (4k_B)$ is the Curie constant for $S = 1/2$, where N_A is the Avogadro constant, μ_0 is the vacuum permeability, μ_B is the Bohr magneton and k_B is the Boltzmann constant. The main features of the $\chi_m(T)$ curve are reasonably well reproduced by this model if a small Curie contribution is also added [Fig. 5(d)]. An unconstrained fit with Eq. (1) yields $J/k_B = 25 \pm 0.3$ K and the effective magnetic moment

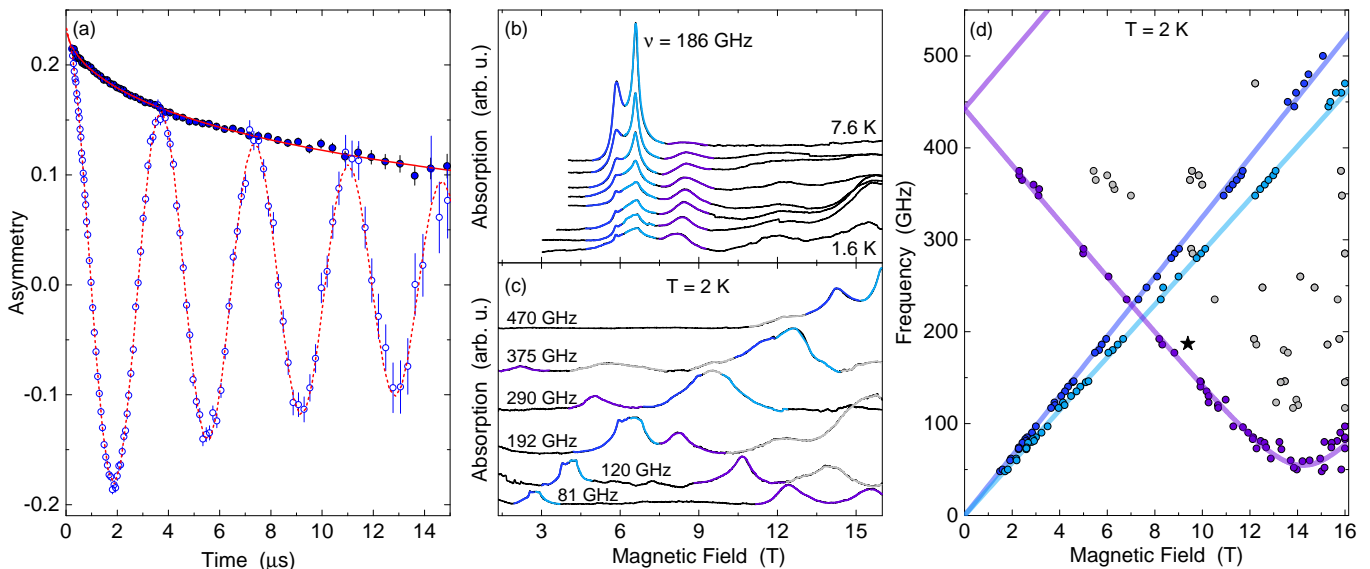


FIG. 7. (a) The zero-field (solid blue circles) and transverse-field (open blue circles) μ SR asymmetry $A(t)$ of Rb_4O_6 powder measured at $T = 1.6$ K. Note the complete absence of oscillations in $A_{ZF}(t)$ in zero applied field, which thus rules out any static order of O_2^- moments down to 1.6 K. The solid red line is a fit to a stretched-exponential relaxation function $A_{ZF}(t) = A_0 \exp[-(\lambda t)^\beta]$ with the initial asymmetry $A_0 = 0.238$ determined in the complementary experiment in the transferred field geometry, relaxation rate $\lambda = 0.046 \mu\text{s}^{-1}$ and the stretching exponent $\beta = 0.54$. (b) Low temperature high-field EPR spectra measured at 186 GHz (from top to bottom at $T = 7.6, 5.5, 4.6, 3.7, 2.8, 2.3, 1.9$ and 1.6 K). The peaks are color-coded to match the modes in the resonance frequency-field diagram – dark and light blue are the conventional EPR lines and purple lines due to the singlet-triplet (ST) transition mode. (c) High-field EPR spectra at 2 K measured at different frequencies. The peaks are color-coded in the same fashion as in (b), with the addition of light gray matching other observed transitions. (d) The resonance frequency-field diagram of Rb_4O_6 measured at 2 K. The dark and light blue circles show the conventional linear dependence characteristic of EPR transitions within the triplet states, the purple circles show the singlet-to-triplet transition modes and the light gray circles are other observed modes of triplet or possibly quintet bound states origin. The black star is the spin gap value determined in NMR measurements.

$\mu_{\text{eff}} = \mu_B g \sqrt{3}/2 = 1.98 \mu_B$. The latter is in good agreement with $\mu_{\text{eff}} = 1.95 \mu_B$ derived from the Curie-Weiss analysis of $\chi_m(T)$ between 50 and 120 K (Fig. S9 in Ref. [26]). The complete disappearance of the main X-band EPR signal at the lowest temperatures fully complies with a spin gap in the excitation spectrum. Moreover, the maximum in $\chi_{\text{EPR}}(T)$ data is also reasonably well matched by Eq. (1), yielding a similar exchange coupling constant $J/k_B = 23 \pm 0.3$ K. All magnetic data thus point to the conclusion that dimers of antiferromagnetically coupled O_2^- spins are the main motif in the magnetic lattice of the Rb_4O_6 low-temperature orbitally ordered $P\bar{4}$ structure.

D. The low-temperature magnetic ground state

To expose the microscopic nature of the magnetic ground state in the low-temperature orbitally-ordered state, i.e. for $T \leq T_s$, we finally resort to multi-frequency EPR measurements. The high resolution of the high-field EPR measurements enables us to resolve the splitting of the EPR spectra below 145 K (Fig. S10 in [26]). On further cooling, the splitting into two well distinct signals at $g_1 = 2.32$ and $g_2 = 2.05$ becomes even more pronounced

[Fig. 7(b)]. This indicates that the slowing down of the O_2 librations opens a path for the structural distortion that is responsible for the two inequivalent O_2^- molecules in the unit cell, which is in excellent agreement with the low-temperature $P\bar{4}$ crystal structure obtained from the PND data [Fig. 1(c) and (d)]. The splitting of the EPR spectra already at temperatures above T_s may be a signature of structural fluctuations, similar to those found in Fe_3O_4 [8].

Similar as in the X-band spectra, the high-field EPR signal intensity reaches a maximum at T_{max} . However, as the intensity of the high-temperature EPR signals starts to decrease, another signal (hereafter labeled as ST) positioned at the resonance field of 8.5 T and well separated from the two main peaks at $g \sim 2$ (i.e., at around 6 T) starts to gradually emerge below 8 K in the experiment conducted at a resonance frequency of 186 GHz, [Fig. 7(b)]. In sharp contrast to the paramagnetic $g \sim 2$ signals, the intensity of the ST signal increases with decreasing temperature.

The appearance of the ST signal in the spin-gapped phase at temperatures well below T_{max} is at first glance surprising and calls for additional frequency-field dependent EPR measurements. Such experiments were conducted at 2 K and are summarized in Figs. 7(c) and (d).

The ST signal displays the opposite frequency-field dependence as compared to the conventional paramagnetic EPR signals at $g_1 = 2.32$ and $g_2 = 2.05$. Namely, with increasing frequency, the ST resonance field decreases. On the resonance frequency-field diagram [Fig. 7(d)], the ST signal shows almost perfect linear dependence that extrapolates to the resonance frequency of 443 GHz at zero field, which corresponds to a zero-field spin gap $\Delta_s(0)/k_B = 21$ K. The spin gap of $\Delta_s(9.39)/k_B = 9$ K, determined in NMR measurements conducted at 9.39 T [Fig. 4 (c)], thus falls nicely on the EPR resonance frequency-field diagram. For fields larger than ~ 13 T, deviations from a simple linear dependence are observed and the resonance field even starts to increase with increasing frequency for fields larger than 14.25 T.

The high-field EPR measurements unambiguously confirm the existence of a zero-field spin gap $\Delta_s(0)$ in the spectrum of low-energy spin excitations. In light of dominant antiferromagnetic interactions, the excitations could, in principle, either be magnons in an antiferromagnetically ordered state, or excitations from the singlet ground state to the triplet excited state. In the former case, the ST signal would be one of the antiferromagnetic resonance (AFMR) modes. However, the μ SR data [Fig. 7(a)] unambiguously rule out any antiferromagnetically ordered state and thus no AFMR signal is expected. On the other hand, the ST signal shows all characteristics of the direct transition from the singlet to the triplet state: the temperature independent zero-field spin gap is given by the dominant antiferromagnetic exchange interaction between two O_2^- spins while the increase of the ST signal intensity with decreasing temperature reflects the increase in the population of the singlet ground state with decreasing temperature. In this picture, the ST resonance frequency-field dependence for fields larger than 13 T, where the triplet branch approaches the singlet energy level, is due to a level anticrossing, which is a hallmark of the Dzyaloshinskii-Moriya (DM) interaction [32]. We stress that this interaction also provides the necessary mixing of quantum spin-states, which makes the direct singlet to triplet transition observable in EPR experiments.

In order to qualitatively describe the magnetic ground state of Rb_4O_6 , we next attempt to fit the EPR resonant field-resonant frequency data. In addition to the dominant antiferromagnetic exchange between pairs of O_2^- spins, we take into account also the DM interaction as the leading magnetic anisotropy term. The latter is symmetry allowed since the center of inversion is absent at the center of each spin dimer in the low-temperature $P\bar{4}$ structure. The complete Hamiltonian for a spin dimer then reads

$$H = JS_1 \cdot S_2 + \mathbf{D} \cdot S_1 \times S_2 + g\mu_B(S_1 + S_2) \cdot \mathbf{B}. \quad (2)$$

Here, \mathbf{D} is the vector of the DM interaction, while the third term accounts for the Zeeman interaction. This model is used to calculate the resonance frequency-field diagram and the best agreement with the experimental

data gives $J/k_B = 21$ K and $D = 2.5$ K [Fig. 7(d)]. The ratio $D/J = 0.12$ is surprisingly large for a light element π -electron system and is for instance of a similar magnitude as typically found in Cu^{2+} systems [32–34].

Although this simple model manages to explain the main features of $\chi_m(T)$, ^{87}Rb NMR and EPR data there are still some details, which may require further weaker terms in Eq. 2. Specifically, the dependence of $\chi_m(T)$ around T_{max} in the magnetic as well as in the EPR susceptibilities shows small deviation from the model predictions. Even when the DM interaction is included in the model for $\chi_m(T)$ [35], it shows only marginal deviation for temperatures below 2 K [Fig. 5(d)]. More importantly, the high-field EPR data show many more peaks, especially at high fields [Fig. 7(b), (c) and (d)], which are also not predicted for the model of isolated dimers. Finally, it is difficult to comprehend that isolated spin dimers would form by the observed small structural change of the otherwise high-temperature tetragonal phase with three-dimensional (3D) pyrochlore exchange network of O_2^- sites [15]. For these reasons we suggest that dimers of O_2^- spins are in fact weakly coupled. If this is the case, then the additional EPR lines observed in the high-field experiments may represent triplet bound states, similar as found in $SrCu_2(BO_3)_2$ [32], which is an archetypal two-dimensional (2D) lattice of interacting dimers. More detailed high-field data in the low-temperature phase is needed, in order to fully understand how the O_2^- dimers interact and form the intricate singlet ground state in Rb_4O_6 .

III. DISCUSSION AND CONCLUSIONS

Similarly as $3d$ -based transition metal compounds, molecule-based alkali sesquioxides A_4O_6 and superoxides AO_2 with partially filled π^* molecular orbitals are a versatile class of compounds for studying strongly correlated electron physics in the presence of orbital degeneracy. In this work we have demonstrated the strong entanglement between spin, charge, orbital, and lattice degrees of freedom in the anionic mixed-valence compound Rb_4O_6 . Just like its sister compound Cs_4O_6 studied before [14], Rb_4O_6 features a Verwey-type charge-ordering transition near 290 K as confirmed here from structural and transport studies. EPR and NMR spectra evidence charge localization on their respective time-scales of 10^{-10} s and 10^{-6} s. The first-order transition from the charge disordered cubic to the charge-ordered tetragonal structures involves a reorientation of the anionic O_2 molecular dumbbells and leads to a tilting of the paramagnetic O_2^- units versus the c -axis. On the other hand, the low-temperature magnetic and structural properties deep in the charge-ordered state of the two Rb- and Cs-based sister compounds are fundamentally different. While the magnetic susceptibility of Cs_4O_6 monotonically increases with decreasing temperature in the absence of any further structural changes [13, 14], Rb_4O_6 shows a pronounced

maximum in $\chi_m(T)$ as well as in $\chi_{\text{EPR}}(T)$ at $T_{\text{max}} \approx 15$ K as a result of dominant antiferromagnetic interactions within pairs of O_2^- spins. The roots of this difference can be traced back to the differences in the orbital ordering patterns. The low-temperature crystal structure derived from the powder neutron diffraction data, the ^{87}Rb NMR spectra and spin-lattice relaxation rates, as well as a g -factor anomaly in the EPR data provide consistent evidence for emergence of a peculiar type of π^* orbital ordering at $T_s = 92$ K, which enables the dominant antiferromagnetic exchange within pairs of O_2^- moments. We stress that the exchange interactions between nearest-neighboring O_2^- spins are known to strongly depend on the precise orbital ordering [16] and thus provide a necessary link between the spin and orbital degrees of freedom.

The importance of the orbital ordering in the charge-ordered state in Rb_4O_6 is evident from our density-functional-theory (DFT) calculations. These calculations for the high-temperature tetragonal structure (space group $I\bar{4}$, Ref. [9]) give the Wannier orbitals and the related hopping integrals between oxygen atoms on the nearest-neighboring dumbbell units. The resulting exchange-coupling network appears to be highly three-dimensional (Table S4 in Ref. [26]), without clear preference for the formation of the antiferromagnetically coupled O_2^- pairs. The formation of such an exchange network seems to be the case in Cs_4O_6 for all temperatures.

On the other hand, Rb_4O_6 undergoes a structural transition at T_s to the $P\bar{4}$ crystal structure, which has pronounced consequences for the underlying orbital order. The calculated partial density of states (PDOS) for selected O_2^- molecules, labeled with numbers from 5 to 12 in Figs. 1(c) and (d), are shown in Fig. S11. They disclose a systematic pattern, where three of spin-up and spin-down states of the two π^* orbitals are almost fully occupied leaving only one of these empty above the Fermi level. PDOS thus exhibit a clear preference for the alternating $\text{O}_2^- \pi_x^*$ and π_y^* orbital order of O_2^- units stacked along the tetragonal c axis [Fig. 1(c) and (d)]. What is remarkable for this structure is that the tilting together with the orbital ordering enables a direct hopping between oxygen atoms of the nearest neighbouring O_2^- units with the strongest hopping between the oxygen atoms on O_2^- pairs 5 – 8, 6 – 12, 7 – 11 and 9 – 10. We note that such hopping pattern is in general agreement with the structural data as these pairs have short end-to-end O-O distances [Fig. 6(c)]. All these hopping integrals are within the precision of our computations nearly the same, i.e., $t^2 = 0.039$ eV² and therefore explain the formation of spin dimers as depicted in Figs. 1(e) and (f). Other direct hopping integrals or pathways that include hopping via O_2^{2-} or Rb p -orbitals are smaller and thus may lead only to the weak exchange coupling between the spin dimers. In order to directly estimate the antiferromagnetic spin dimer exchange coupling, J , we next calculate the total energies of the two magnetic configurations: the one with the antiferromagnetic alignment of

O_2^- spins on the spin dimers 5 – 8, 6 – 12, 7 – 11 and 9 – 10, and the one with the ferromagnetic alignment of all spins. By comparing the relative energies of these two magnetic configurations (Table S5 in Ref. [26]), we compute the intra-dimer exchange $J = 30.7$ K, which is in reasonable agreement with the experimental data [Figs. 5(d) and 7(d)]. The small discrepancy between the experimental and DFT values of J may partly arise from the neglected inter-dimer exchange.

The observed coupling between the orbital and spin degrees of freedom may be in Rb_4O_6 facilitated through two different physical mechanisms. The first mechanism involves a Kugel-Khomskii-type behavior [23], where the orbital ordering is driven by exchange interactions. We note that the Kugel-Khomskii model was successfully applied to cuprates with degenerate e_g orbitals, such as for example KCuF_3 or K_2CuF_4 [24], but rarely to π electron systems. Alternatively, the compressed lattice in Rb_4O_6 compared to Cs_4O_6 could trigger an instability of the high-temperature tetragonal $I\bar{4}$ structure via an additional rotation of the O_2^- units and result in a lowering of the structural symmetry to $P\bar{4}$ and concomitant increasing in the crystal-field splitting between the π^* orbitals. The magnetic interactions giving rise to spin dimerization then would be rather a consequence of the structural instability. We stress that the relative importance of the Kugel-Khomskii-type exchange and Jahn-Teller-like electron-lattice coupling is currently an important subject for understanding orbital-ordering phenomena [20, 36].

The interplay between the Kugel-Khomskii-type superexchange, crystal-field splitting, spin-orbit coupling (SOC), and the resulting orbital-ordering patterns was theoretically analyzed for the monovalent superoxide KO_2 [22], where a series of structural transitions involving different types and degrees of tilting of the O_2^- units was observed. For the small tilting angles of the O_2^- units versus the c axis in the basic tetragonal structure the Kugel-Khomskii mechanism together with SOC dominates, whereas for larger tilting angles the crystal-field splitting becomes more important. For intermediate angles competition between the various interactions occurs. Our structural studies reveal a quite large tilting angle of $\sim 20^\circ$ for Rb_4O_6 in the $I\bar{4}$ and $\sim 28^\circ$ in the $P\bar{4}$ structure, which is even enhanced compared to that of $\sim 17^\circ$ in Cs_4O_6 . Thus, based on Ref. [22], the crystal-field splitting of the degenerate π^* molecular orbitals is expected to stabilize the tetragonal $I\bar{4}$ charge-ordered structures in both, Rb_4O_6 and Cs_4O_6 . The larger tilting angle indicates larger orbital splitting in Rb_4O_6 than in Cs_4O_6 which is in agreement with the persistence of the tetragonal structure to higher temperatures in Rb_4O_6 . The final remaining question is about the driving force of the orbital ordering transition at $T_s = 92$ K. Here, as the temperature is significantly lower, the Kugel-Khomskii mechanism could play an important role and open the path for an additional structural adaptation by rotation of the O_2^- units and spin dimer forma-

tion. A theoretical modeling of the sesquioxides incorporating also the hopping terms due to the mixed-valence situation is highly desirable to resolve the nature of the different structural transitions and especially to clarify the detailed role of Jahn-Teller-like structural distortions and Kugel-Khomskii-type exchange in orbital ordering of mixed-valence strongly correlated electron systems with orbital degeneracy [20, 36].

The present comprehensive study of the anionic π -electron mixed-valence compound Rb_4O_6 unambiguously demonstrates, how lattice, charge, orbital and spin degrees of freedom couple and tune the ground state in alkali sesquioxides. In this respect alkali sesquioxides are reminiscent of many notable mixed-valence d -electron systems, such as cuprates, manganites and Fe_3O_4 or more complex p -electron systems like fullerides [37]. In Fe_3O_4 , the charge and orbital ordering leads to an interesting magnetic ground state of coupled trimerons [7, 8] – a highly complex spin formation deep in the Verwey phase. The low-temperature EPR spectra in Rb_4O_6 may yield evidences for analogous structural/orbital/spin fluctuations inherent to charge-ordered π electron alkali sesquioxides. In these light element molecular solids, the natural frequencies of spin excitations are lowered and thus become accessible to most spectroscopic methods. Studying mixed-valence alkali sesquioxides may thus in the future provide deeper understanding of the complex excitations in Verwey-type compounds. Finally, the lack of long-range magnetic order as apparent from the present ZF μSR measurements down to 1.6 K suggests that also the quantum magnetism of this class of compounds deserves further attention.

ACKNOWLEDGEMENTS

We thank Patrick Merz for preparation of the samples, Ralf Koban and Walter Schnelle for the magnetization measurements, and Jrg Daniels for assistance with structural drawings. In initial stages of the project were supported by the European Union FP7-NMP-2011-EU-Japan project LEMSUPER under contract no. 283214. This work was supported by the Deutsche Forschungsgemeinschaft (DFG), through ZV 6/2-2, and by the HLD at HZDR, member of the European Magnetic Field Laboratory (EMFL). D.A. acknowledges financial support from the Slovenian Research Agency (Core Research Funding No. P1-0125 and projects No. J1-9145 and N1-0052). Experiments at the ISIS Neutron and Muon Source were supported by a beamtime allocation RB1820363 from the Science and Technology Facility Council. These measurements are available in Ref. [38].

METHODS

Rb_4O_6 was prepared by thermal decomposition of the superoxide RbO_2 as described in Ref. [39]. The purity

of the samples was checked by laboratory powder x-ray diffraction (XRD) measurements using monochromatic $\text{CuK}_{\alpha 1}$ radiation. Due to the extreme air and moisture sensitivity of alkali metal oxides, all sample handlings were carried out under carefully controlled inert atmospheres.

Powder neutron diffraction (PND) experiments on Rb_4O_6 were carried out on the instruments E6 and E9 at the BER II reactor of the Helmholtz-Zentrum Berlin. These instruments use a pyrolytic graphite (PG) and a Ge-monochromator selecting the neutron wavelengths $\lambda = 2.426 \text{ \AA}$ (E6) and $\lambda = 1.7985 \text{ \AA}$ (E9), respectively. For the PND experiments, about 4 g of Rb_4O_6 powder, which was sealed in a thin-walled quartz tube and then placed in a vanadium can (6 mm diameter), was used. Powder data of Rb_4O_6 were collected on E6 between the diffraction angles 8 and 136.5° and on E9 between 8 and 141.8° . On the instrument E9 full data sets of Rb_4O_6 were collected at 3, 100 and 400 K to determine precisely the positional parameters of the cubic and tetragonal structures, respectively. The refinements of the crystal structures were carried out with the program FullProf [40] with the nuclear scattering lengths $b(\text{O}) = 5.805 \text{ fm}$ and $b(\text{Rb}) = 7.09 \text{ fm}$ [41].

On the instrument E6 we have investigated in detail the structural changes as a function of temperature in the range from 3 to 427 K. For all experiments we have used an Orange Cryofurnace (AS Scientific Products Ltd., Abingdon, GB). Considering that the structural and electronic properties of alkali sesquioxides sensitively depend on the thermal protocol [13] two different types of PND experiments were performed. In the first one the virgin sample was heated to above 400 K and then subsequently cooled down slowly. Between 250 and 380 K the cooling rates were kept to 1 K/min. Finally, the sample was cooled down to base temperature (2 K) and the sample was subsequently heated up again to 400 K. At selected temperatures PND patterns were collected with a measurement time of about 35 min at E6 and of 20 hrs at E9. In a second fast cooling experiment the sample was quenched into liquid nitrogen from 400 down to 80 K with an average cooling rate of about 40 K per minute. Then it was further cooled down to 3 K in the cryostat with a cooling rate of 2-3 K per minute. Subsequently the sample was heated up again, where the set temperatures for data collection were reached within 10 minutes.

Impedance measurements were performed on Rb_4O_6 pellets having a diameter of 6 mm and a thickness of around 1 mm following the experimental and data evaluation procedures described in Ref. [14]. The measurements were carried out in a temperature range of 363 to 200 K in steps of 5 K during slow cooling down to 200 K and the subsequent also on heating using the same temperature step.

Magnetization measurements on powders of Rb_4O_6 sealed in a Suprasil quartz tube were performed with an MPMS3 (Quantum Design) magnetometer in field-

cooling and field-heating modes in a magnetic field of 0.1 T. Starting from 400 K where the sample is entirely in the cubic phase, the sample was cooled with a rate of 2 K/min down to 2 K and subsequently heated back to 400 K at the same rate.

Zero-field (ZF) muon spin relaxation (μ SR) experiments were performed in an Oxford Instruments Variox cryostat on the MUSR instrument (ISIS, Rutherford Appleton Laboratory, United Kingdom) after slow cooling of the Rb_4O_6 sample to low temperatures. The sample was protected against the exposure to air in a home-made sample container.

Continuous wave X-band EPR measurements were done using a home-built spectrometer equipped with a Varian E-101 microwave bridge operating at 9.37 GHz, a Varian TEM104 dual cavity resonator, an Oxford Instruments ESR900 cryostat and an Oxford Instruments ITC503 temperature controller with temperature stability better than $\pm 0.05\text{K}$ at all temperatures. For the purpose of the measurements, the sample was sealed in a Suprasil quartz tube (Wilmad-LabGlass, 4 mm medium wall tube) under dynamic vacuum.

High-Field EPR measurements were done at the Dresden High Magnetic Field Laboratory (HLD) in the Helmholtz Zentrum Dresden Rossendorf. The experiments were performed using a multifrequency transmission-type EPR spectrometer equipped with a 16 T superconducting magnet in a Faraday configuration, similar to that described in Ref. [42]. In our experiments, a set of VDI microwave sources were used, allowing us to probe magnetic excitations in this material in the quasi-continuously covered frequency range from approximately 50 to 500 GHz. The thermal protocol included slow cooling to base temperature $T = 1.6\text{ K}$. The sample was the same as in X-band EPR experiments.

NMR measurements of the ^{87}Rb ($I = 3/2$) frequency-swept spectra were done in a 4.7 T superconducting magnet. We used a standard solid-echo pulse sequence $(\pi/2) - \tau - (\pi/2) - \tau$ and appropriate phase cycling. The radio-frequency pulse length was optimized to $t_{\pi/2} = 3.2\ \mu\text{s}$ and the interpulse-delay was set to $\tau = 50\ \mu\text{s}$. Typical repetition time was 20 ms. The complete wide-line polycrystalline NMR spectrum was obtained by summing the real part of individual spectra measured step by step at resonance frequencies separated by $\Delta\nu = 50\ \text{kHz}$. The spin-lattice and spin-spin relaxation rates were measured using a 9.39 T magnet with the inversion-recovery technique. All NMR measurements were performed in the temperature range between 5 and 380 K using a slow cooling protocol.

DFT calculations were done by applying the Quantum Espresso code [43]. The exchange-correlation effects were calculated by means of the generalized-gradient approximation [44] with explicitly added [45] Hubbard repulsion term $U = 4.1\ \text{eV}$ for the oxygen atoms. The electron-ion interactions were described with the gauge-including-projected-augmented-waves (GIPAW) pseudopotentials [46, 47] making us possible to calculate the NMR-based quantities. The plane waves and the charge-density cutoff parameters were set to 639 eV and 2543 eV, respectively, whereas a $4 \times 4 \times 4$ mesh of \mathbf{k} -points [48] was used for the Brillouin-zone integration. The self-consistent criterion was the total-energy difference between the two subsequent calculations being less than $10^{-6}\ \text{Ry}$. In order to initially estimate the exchange coupling between particular oxygen dumbbell units, we determined the hopping integrals between the corresponding maximally-localized Wannier orbitals, which resulted from the wannierization performed with the Wannier90 tool [49].

-
- [1] M. B. Robin, "The color and electronic configurations of prussian blue," *Inorg. Chem.* **1**, 337–342 (1962).
- [2] C. N. R. Rao and B. Raveau, *Colossal Magnetoresistance, Charge Ordering and Related Properties of Manganese Oxides* (World Scientific, Singapore, 1998).
- [3] M. Uehara, S. Mori, C. H. Chen, and S.-W. Cheong, "Percolative phase separation underlies colossal magnetoresistance in mixed-valent manganites," *Nature* **399**, 560 (1999).
- [4] J. Chang, E. Blackburn, A. T. Holmes, N. B. Christensen, J. Larsen, J. Mesot, R. Liang, D. A. Bonn, W. N. Hardy, and A. Watenphul et al., "Direct observation of competition between superconductivity and charge density wave order in $\text{YBa}_2\text{Cu}_3\text{O}_{6.67}$," *Nat. Phys.* **8**, 871 (2012).
- [5] E. J. W. Verwey, "Electronic conduction of magnetite (Fe_3O_4) and its transition point at low temperatures," *Nature* **144**, 327 (1939).
- [6] E. J. Verwey, P. W. Haayman, and F. C. Romeijn, "Physical properties and cation arrangement of oxides with spinel structures ii. electronic conductivity," *J. Chem. Phys.* **15**, 181–187 (1947).
- [7] M. S. Senn, J. P. Wright, and J. P. Attfield, "Charge order and three-site distortions in the Verwey structure of magnetite," *Nature* **481**, 173 (2012).
- [8] G. Perversi, E. Pachoud, J. Cumby, J. Hudspeth, J. P. Wright, S. A. J. Kimber, and J. P. Attfield, "Co-emergence of magnetic order and structural fluctuations in magnetite," *Nat. Commun.* **10**, 2857 (2019).
- [9] A. Sans, J. Nuss, G. H. Fecher, C. Mühle, C. Felser, and M. Jansen, "Structural implications of spin, charge, and orbital ordering in rubidium sesquioxide, Rb_4O_6 ," *Z. Anorg. Allg. Chem.* **640**, 1239–1246 (2014).
- [10] M. Jansen, R. Hagenmayer, and N. Korber, " Rb_4O_6 studied by elastic and inelastic neutron scattering: In memoriam Jean Rouxel," *Cr. Acad. Sci. II C* **2**, 591–594 (1999).
- [11] M. Jansen and N. Korber, "Neue untersuchungen zu präparation und struktur von Rb_4O_6 ," *Z. Anorg. Allg. Chem.* **598**, 163–173 (1991).
- [12] A. Helms and W. Klemm, "Über die kristallstrukturen der rubidium-und cäsiumsesequioxyde," *Z. Anorg. Allg.*

- Chem. **242**, 201–214 (1939).
- [13] D. Arčon, K. Anderle, M. Klanjšek, A. Sans, C. Mühle, P. Adler, W. Schnelle, M. Jansen, , and C. Felser, “Influence of O₂ molecular orientation on *p*-orbital ordering and exchange pathways in Cs₄O₆,” Phys. Rev. B **88**, 224409 (2013).
- [14] P. Adler, P. Jeglič, M. Reehuis, M. Geiß, P. Merz, T. Knaflič, M. Komelj, A. Hoser, A. Sans, and J. Janek et al., “Verwey-type charge ordering transition in an open-shell *p*-electron compound,” Sci. Adv. **4**, eaap7581 (2018).
- [15] R. H. Colman, H. E. Okur, W. Kockelmann, C. M. Brown, A. Sans, C. Felser, M. Jansen, and K. Prassides, “Elusive Valence Transition in Mixed-Valence Sesquioxide Cs₄O₆,” Inorg. Chem. **58**, 14532 (2019).
- [16] S. Riyadi, B. Zhang, R. A. de Groot, A. Caretta, P. H. M. van Loosdrecht, T. T. M. Palstra, and G. R. Blake, “Antiferromagnetic $s = 1/2$ spin chain driven by *p*-orbital ordering in CsO₂,” Phys. Rev. Lett. **108**, 217206 (2012).
- [17] M. Klanjšek, D. Arčon, A. Sans, P. Adler, M. Jansen, and C. Felser, “Phonon-modulated magnetic interactions and spin tomonaga-luttinger liquid in the *p*-orbital antiferromagnet CsO₂,” Phys. Rev. Lett. **115**, 057205 (2015).
- [18] T. Knaflič, M. Klanjšek, A. Sans, P. Adler, M. Jansen, C. Felser, and D. Arčon, “One-dimensional quantum antiferromagnetism in the *p*-orbital CsO₂ compound revealed by electron paramagnetic resonance,” Phys. Rev. B **91**, 174419 (2015).
- [19] S. Kadota, I. Yamada, S. Yoneyama, and K. Hirakawa, “Formation of one-dimensional antiferromagnet in KCuF₃ with the perovskite structure,” J. Phys. Soc. Jpn. **23**, 752 (1967).
- [20] E. Pavarini, E. Koch, and A. I. Lichtenstein, “Mechanism for orbital ordering in KCuF₃,” Phys. Rev. Lett. **101**, 266405 (2008).
- [21] F. Astuti, M. Miyajima, T. Fukuda, M. Kodani, T. Nakano, T. Kambe, , and I. Watanabe, “Aniogenic magnetism combined with lattice symmetry in alkali-metal superoxide RbO₂,” J. Phys. Soc. Jpn. **88**, 043701 (2019).
- [22] M. Kim and B. I. Min, “Temperature-dependent orbital physics in a spin-orbital-lattice-coupled *2p*-electron Mott system: The case of KO₂,” Phys. Rev. B **89**, 121106(R) (2014).
- [23] K. I. Kugel and D. I. Khomskii, “Crystal structure and magnetic properties of substances with orbital degeneracy,” Zh. Eksp. Teor. Fiz. **64**, 1429 (1973).
- [24] A. M. Oleś, “Orbital physics,” arXiv preprint arXiv:1708.07183 (2017).
- [25] J. Winterlik, G. H. Fecher, C. A. Jenkins, C. Felser, C. Mühle, K. Doll, M. Jansen, L. M. Sandratskii, and J. Kübler, “Challenge of magnetism in strongly correlated open-shell *2p* systems,” Phys. Rev. Lett. **102**, 016401 (2009).
- [26] “Supplemental material,” .
- [27] W. Känzig and M. H. Cohen, “Paramagnetic resonance of oxygen in alkali halides,” Phys. Rev. Lett. **3**, 509–510 (1959).
- [28] A. Bencini and D. Gatteschi, *EPR of Exchange Coupled Systems* (Springer, Heidelberg, 1990).
- [29] J. Winterlik, G. H. Fecher, C. A. Jenkins, S. Medvedev, C. Felser, J. Kübler, C. Mühle, K. Doll, M. Jansen, and T. Palasyuk et al., “Exotic magnetism in the alkali sesquioxides Rb₄O₆ and Cs₄O₆,” Phys. Rev. B **79**, 214410 (2009).
- [30] A.G.E Schenck, *Muon Spin Rotation Spectroscopy: Principles and Applications in Solid State Physics* (Taylor & Francis, 1985).
- [31] B. Bleaney and K. D. Bowers, “Anomalous paramagnetism of copper acetate,” Proc. R. Soc. Lond. A **214**, 451–465 (1952).
- [32] H. Nojiri, H. Kageyama, Y. Ueda, and M. Motokawa, “Esr study on the excited state energy spectrum of SrCu₂(BO₃)₂—a central role of multiple-triplet bound states,” J. Phys. Soc. Jpn. **72**, 3243–3253 (2003).
- [33] A. Zorko, S. Nellutla, J. van Tol, L. C. Brunel, F. Bert, F. Duc, J.-C. Trombe, M. A. de Vries, A. Harrison, and P. Mendels, “Dzyaloshinsky-Moriya anisotropy in the spin-1/2 kagome compound ZnCu₃(OH)₆Cl₂,” Phys. Rev. Lett. **101**, 026405 (2008).
- [34] A. Zorko, F. Bert, A. Ozarowski, J. van Tol, D. Boldrin, A. S. Wills, and P. Mendels, “Dzyaloshinsky-Moriya interaction in vesignieite: A route to freezing in a quantum kagome antiferromagnet,” Phys. Rev. B **88**, 144419 (2013).
- [35] S. Stoll and A. Schweiger, “Easyspin, a comprehensive software package for spectral simulation and analysis in epr,” J. Magn. Reson. **178**, 42–55 (2006).
- [36] E. Pavarini and E. Koch, “Origin of Jahn-Teller distortion and orbital ordering in LaMnO₃,” Phys. Rev. Lett. **104**, 086402 (2010).
- [37] G. Klupp, P. Matus, K. Kamerás, A. Y. Ganin, A. McLennan, M. J. Rosseinsky, Y. Takabayashi, M. T. McDonald, and K. Prassides, “Dynamic Jahn-Teller effect in the parent insulating state of the molecular superconductor Cs₃C₆₀,” Nat. Commun. **3**, 912 (2012).
- [38] D. Arčon et al., “Valence bond solid in the charge ordered state of Rb₄O₆,” (2019), <https://doi.org/10.5286/ISIS.E.RB1820363>.
- [39] P. Merz, M. Schmidt, C. Felser, and M. Jansen, “Thermo-analytical investigations on the superoxides AO₂ (A = K, Rb, Cs) revealing facile access to sesquioxides A₄O₆,” Z. Anorg. Allg. Chem. **643**, 544 (2017).
- [40] J. Rodríguez-Carvajal, “Recent advances in magnetic structure determination by powder neutron diffraction,” Physica B **192**, 55 (1993).
- [41] V. F. Sears, *International Tables for Crystallography*, Vol. C (Kluwer Academic Publisher, 1995).
- [42] S. A. Zvyagin, J. Krzystek, P. H. M. van Loosdrecht, G. Dhalenne, and A. Revcolevschi, “High-field ESR study of the dimerized-incommensurate phase transition in the spin-peierls compound CuGeO₃,” Physica B **346-347**, 1 (2004).
- [43] P. Giannozzi, S. Baroni, N. Bonini, M. Calandra, R. Car, C. Cavazzoni, D. Ceresoli, G. L. Chiarottia, M. Cococcioni, and I. Dabo et al., “Quantum espresso: a modular and open-source software project for quantum simulations of materials,” J. Phys. Condens. Matter **21**, 395502 (2009).
- [44] J. P. Perdew, K. Burke, and M. Ernzerhof, “Generalized gradient approximation made simple,” Phys. Rev. Lett. **77**, 3865–3868 (1996).
- [45] M. Cococcioni and S. de Gironcoli, “Linear response approach to the calculation of the effective interaction parameters in the LDA + U method,” Phys. Rev. B **71**, 035105 (2005).
- [46] C. J. Pickard and F. Mauri, “All-electron magnetic response with pseudopotentials: NMR chemical shifts,”

- Phys. Rev. B **63**, 245101 (2001).
- [47] A. Dal Corso, “Pseudopotentials periodic table: From H to Pu,” *Comput. Mater. Sci.* **95**, 337 (2014).
- [48] H. J. Monkhorst and J. Pack, “Special points for Brillouin-zone integrations,” *Phys. Rev. B* **13**, 5188 (1976).
- [49] A. A. Mostofi, J. R. Yates, Y.-S. Lee, I. Souza, D. Vanderbilt, and N. Marzari, “wannier90: A tool for obtaining maximally-localised Wannier functions,” *Comput. Phys. Commun.* **178**, 685 (2008).

Spin-dimer ground state driven by consecutive charge and orbital ordering transitions in the anionic mixed-valence compound Rb_4O_6

Supplemental information

T. Knaflič,¹ P. Jeglič,¹ M. Komelj,¹ A. Zorko,^{1,2} P. K. Biswas,³ A. N. Ponomaryov,⁴ S. A. Zvyagin,⁴ M. Reehuis,⁵ A. Hoser,⁵ M. Geiß,⁶ J. Janek,⁶ P. Adler,^{7,*} C. Felser,⁷ M. Jansen,^{7,#} and D. Arčon^{1,2,§}

¹Jožef Stefan Institute, Jamova c. 39, 1000 Ljubljana, Slovenia

²Faculty of Mathematics and Physics, University of Ljubljana, Jadranska c. 19, 1000 Ljubljana, Slovenia

³ISIS Pulsed Neutron and Muon Source, STFC Rutherford Appleton Laboratory, Didcot OX11 0QX, UK

⁴Dresden High Magnetic Field Laboratory (HLD-EMFL), Helmholtz-Zentrum Dresden-Rossendorf, 01328 Dresden, Germany

⁵Helmholtz-Zentrum Berlin für Materialien und Energie, 14109 Berlin, Germany

⁶Institute of Physical Chemistry and Center for Materials Research, Justus-Liebig- University Giessen, Heinrich-Buff-Ring 17, 35392 Giessen, Germany

⁷Max Planck Institute for Chemical Physics of Solids, Nöthnitzer Straße 40, 01187 Dresden, Germany

* adler@cpfs.mpg.de

m.jansen@fkf.mpg.de

§ denis.arcon@ijs.si

Refinement of high-resolution powder neutron diffraction patterns

Powder neutron diffraction (PND) investigation show that Rb_4O_6 undergoes a structural transition from the cubic (space group $I\bar{4}3d$, No. 220) to the tetragonal (space group $I\bar{4}$, No. 82) crystal structure. Structural transition starts at around $T = 290$ K and is nearly completed at $T = 250$ K. The temperature dependence of the fractions of the cubic and tetragonal phase in the slow cooling mode is derived from the Rietveld refinements of data collected on instrument E6 at the BER II reactor of the Helmholtz-Zentrum Berlin and is shown in Fig. S1.

The results of the Rietveld refinements of the data collected at instrument E9 are shown in Fig. S2. The high-temperature cubic crystal structure of Rb_4O_6 was refined in the space group $I\bar{4}3d$ (No. 220). For the Rietveld refinements of the PND pattern collected at 400 K, we have used the values from the x-ray data of cubic Rb_4O_6 (Ref. [29] in the main text) as starting values. In this setting the Rb and O atoms are located at the Wyckoff position $16c(x,x,x)$ and $24d(x',0,1/4)$ [in our case $(x,0,3/4)$ with $x = 1/2 - x'$], respectively. The refinement of the positional parameters $x(\text{Rb})$ and $x(\text{O})$ as well as of the two thermal parameters resulted in a somewhat enlarged residual $R_F = 0.106$ (defined as $R_F = \sum ||F_{\text{obs}}| - |F_{\text{calc}}|| / \sum |F_{\text{obs}}|$). This can be ascribed to the fact that the strongly enlarged thermal parameters lead to a strong continuous decrease of the intensity of Bragg reflections up to

higher scattering angles as it can be seen in Fig. S2, top. However, the positional and thermal parameters could be determined to a good accuracy. For the data set collected at 100 K a much smaller residual $R_F = 0.043$ was obtained, because of the much higher intensity of the high-order Bragg reflections (Fig. S2, bottom). At this temperature the crystal structure of the dominating tetragonal phase of Rb_4O_6 was refined in the space group $I\bar{4}$ (No. 82). The two crystallographically distinct atoms Rb1 and Rb2 occupy the Wyckoff positions $8g(x,y,z)$, while the O atoms are located at the following positions: O1 at $4e(0,0,z)$, O2 at $4f(0,1/2,z)$ and both O3 and O4 at $8g(x,y,z)$. In the refinements we have considered the two types of anions (O_2^{2-} and O_2^- as rigid groups, where a soft constraint was applied by setting a standard deviation of the ideal value of the bond distance d (in our case a ratio of $\sigma/d = 0.001$). For the peroxide and superoxide anions, O_2^{2-} (atoms labeled as O1 and O2) and O_2^- (atoms labeled as O3 and O4), we have obtained the bond distances 1.524(4) and 1.312(7) Å, which are slightly smaller than the ideal values of 1.54 and 1.33 Å, respectively. At 2.9 K additional Bragg reflections were found obeying the extinction rule $h + k + l = 2n + 1$. This clearly suggests the loss of the I -centered symmetry. Therefore, we carried out the crystal-structure refinements in the next-lower symmetric space group $P\bar{4}$ (No. 81) which resulted in a satisfactory residual $R_F = 0.041$. In this space group each atom site splits into the following Wyckoff positions: two sites $4h(x,y,z)$ for O3, O4 and all Rb atoms; $2e(0,0,z)$ and $2f(1/2,1/2,z)$ for O1; two sites $2g(0,1/2,z)$ for O2.

In the cubic phase one only finds one single bond length for the O_2 units. Due to the fact that the concentration ratio of the O_2^- and O_2^{2-} anions is exactly two the average charge of the O_2 units is $-4/3$. Therefore, we expect an average bond length of 1.40 Å. From our unrestricted refinements we have obtained a reduced bond length of 1.256(3) Å at 400 K. Accordingly, in the refinement, similar as in the refinement of the tetragonal structure, a constraint was used and an ideal O-O bond length of 1.40 Å was taken as starting value. Finally, bond lengths of 1.350(4) Å were obtained. It has to be mentioned that the residual R_F of the cubic structure was slightly increased from 0.103 to 0.106 by using this constraint. On the other hand, the residual $R_F = 0.043$ for the tetragonal structure remained practically unchanged. The results of the refinements are summarized in Tables S1 and S2 as well as in Fig S2.

In a control PND experiment run at instrument E6 ($\lambda = 2.426$ Å), we have applied a rapid cooling procedure: the Rb_4O_6 sample was quenched into liquid nitrogen from 400 down to 80 K with an average cooling rate of about 40 K per minute. Then it was further cooled down to 3 K in the cryostat with a cooling rate of 2-3 K per minute. The pattern collected at 2 K matches (Fig. S3) the cubic structure, which is thus almost completely frozen-in in such quench cooling experiments.

Impact of different cooling protocols

In measurements of the static molar susceptibility, $\chi_m(T)$, we tested the influence of different cooling protocols on the magnetic properties (Fig. S5). In the slow cooling experiment, a cooling rate of 2 K/min was applied starting from 400 K, while in the rapid cooling procedure a cooling rate of 20 K/min was applied.

In continuous wave X-band electron paramagnetic resonance (EPR) experiments, we always found a residual signal at low temperatures (Fig. S6), that is markedly different from the much broader EPR signal of the tetragonal phase (Fig. 5 in the main text). This signal can be fitted to a lineshape with g -factor anisotropy. The fit converged to the axially-symmetric g -factor anisotropy yielding $g_x = g_y = 1.9757$ and $g_z = 2.3110$ and a small Lorentzian broadening of $\Delta B_x = \Delta B_y = 29.2$ mT and $\Delta B_z = 33.3$ mT. In the lineshape fitting procedure a broad background signal was added with $g = 2.0242$ and $\Delta B = 247$ mT.

X band EPR measurements

Quench experiment

The Rb_4O_6 powder sample (the same one as used in all other EPR experiments), was in these set of experiments first heated to 400 K for an extended period in order to ensure 100% cubic phase. The sample was then directly submerged into liquid nitrogen and was after thermalization quickly transferred into a pre-cooled EPR He-flow cryostat at 100 K. The sample was then rapidly cooled down to base temperature of 3.4 K in several minutes. The X band EPR measurements were then conducted on heating. According to powder neutron diffraction results (Fig. S3), such thermal protocol ensures that the cubic phase is completely frozen in at low temperatures. With increasing temperature, the cubic phase remains metastable up to 160 K, where the tetragonal phase starts to appear.

X-band EPR spectra of the quenched cubic phase appear as a very broad Lorentzian line with a linewidth of 830 mT at 3.4 K (Fig. S7). With increasing temperature, the EPR spectra become even broader, while the EPR signal intensity decreases (Fig. S8). The EPR signal intensity follows the Curie-Weiss law with a small Curie temperature (inset to Fig. S8). Above ~ 50 K the spectral linewidth exceeds 1 T and as a result measurements of EPR spectra become difficult. The broadening trend continues and together with decreasing intensity, we could extract at best only rough estimates of spectral parameters. However, above 157 K the X-band EPR signal suddenly reappears [Fig. S7(c)], marking the transition from the metastable cubic to the tetragonal phase. The reappearance of tetragonal EPR signal above 157 K thus corroborates the powder neutron diffraction data (Fig. 2 (b), main text). Above 157 K, the linewidth and the g -factor of the EPR spectra follow again the trend from the measurements of the tetragonal phase taken during the slow-cooling experiments (main text).

Impedance spectroscopy and transport data

Rb₄O₆ pellets with a diameter of 6 mm and a thickness of around 1 mm were pressed for impedance measurements. Gold foil with a diameter of 6 mm as electrodes was fixed to the two sides of the Rb₄O₆ pellets. The pellets were connected with nickel tabs as current collectors and were sealed in gas-tight pouch foil in an argon-filled glovebox [MBRAUN, < 0.1 parts per million (ppm) H₂O, < 0.1 ppm O₂]. Temperature-dependent impedance measurements were then carried out using an Alpha-A mainframe by Novocontrol Technologies with an equipped POT/GAL30V2A electrochemical test station and a ZG4 test interface. The measurements were carried out in a temperature range of 373 K to 173 K in steps of 5 K. The temperature was adjusted using a liquid nitrogen-based cooling system and a heating coil. The sample holder was placed in a steel vessel, where it was cooled in the nitrogen gas flow. For each temperature step, a relaxation time of 2.5 hours was chosen with a maximum temperature change of 0.3 K/min. The impedance was measured between 10 MHz and 10 mHz with a sinus amplitude of 10 mV. Data evaluation was performed using the software RelaxIS 3 (rhd instruments). For fitting the data, an equivalent circuit consisting of a parallel resistor R and a constant phase element Q was chosen. From the resulting resistances, the electrode area and the thickness of the sample, temperature-dependent conductivities σ_{el} were calculated. Due to the high resistance of the sample, conductivities at temperatures below 203 K could not be determined.

The impedance measurement can be used to derive further transport properties. Assuming a charge carrier density n of $4/V_{\text{cell}}$ (V_{cell} represents the unit cell calculated from the lattice parameters given in Fig. 2), the electron mobility u as a function of temperature (Fig. S11) can be calculated from the electronic conductivity σ_{el} as $u = \frac{\sigma_{el}}{e_0 \cdot n}$, with the electron charge e_0 . Because the electron concentration changes only due to the thermal lattice expansion, the dramatic jump in conductivity directly represents a jump of the electron mobility. Using the Nernst-Einstein relation $D = \frac{u \cdot k_B \cdot T}{e_0}$, the diffusion coefficient D can be retrieved from the mobility using the Boltzmann constant k_B and the absolute temperature T (Fig. S12).

Assuming isotropic diffusion of the electrons, the diffusion coefficient D is related to the jump distance a and the jump frequency ω according to $D = 1/6 \cdot a^2 \cdot \omega$. For the jump distance, the shortest intermolecular distance between the oxygen dumbbells was used. This results in $a = 439$ pm for the cubic structure and $a = 411$ pm for the tetragonal structure, leading to the jump frequency in Fig. S13.

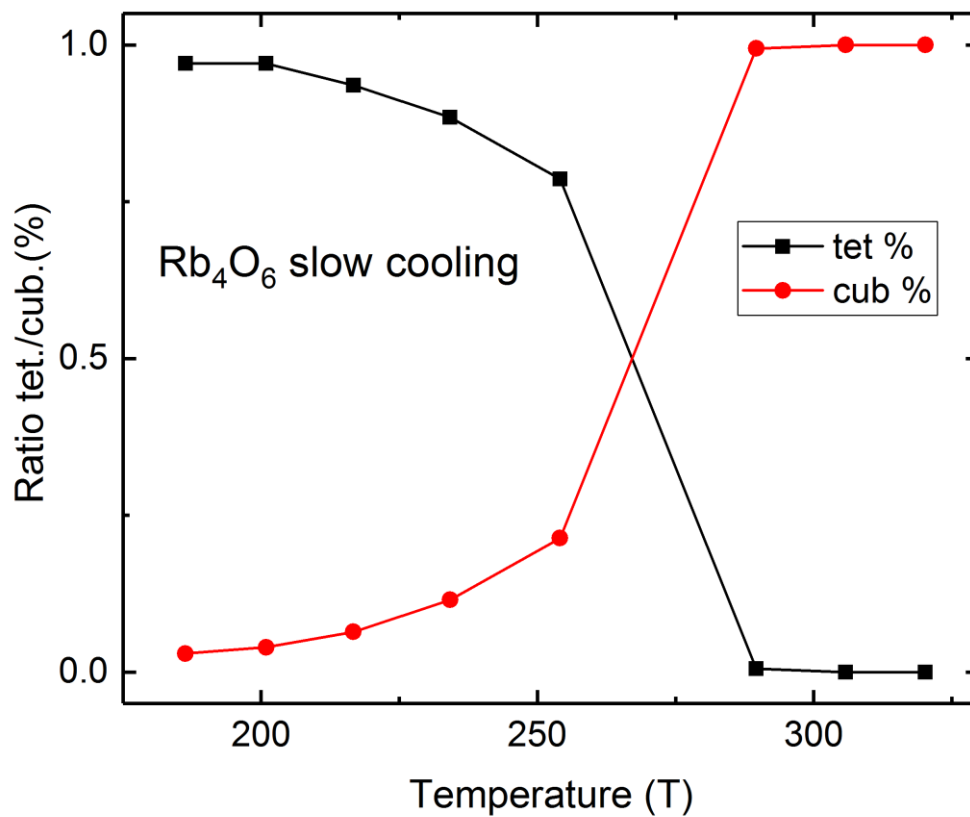


FIG. S1 Temperature dependence of the fractions of the cubic and tetragonal phases in the slow cooling mode derived from the Rietveld refinements of data collected on instrument E6.

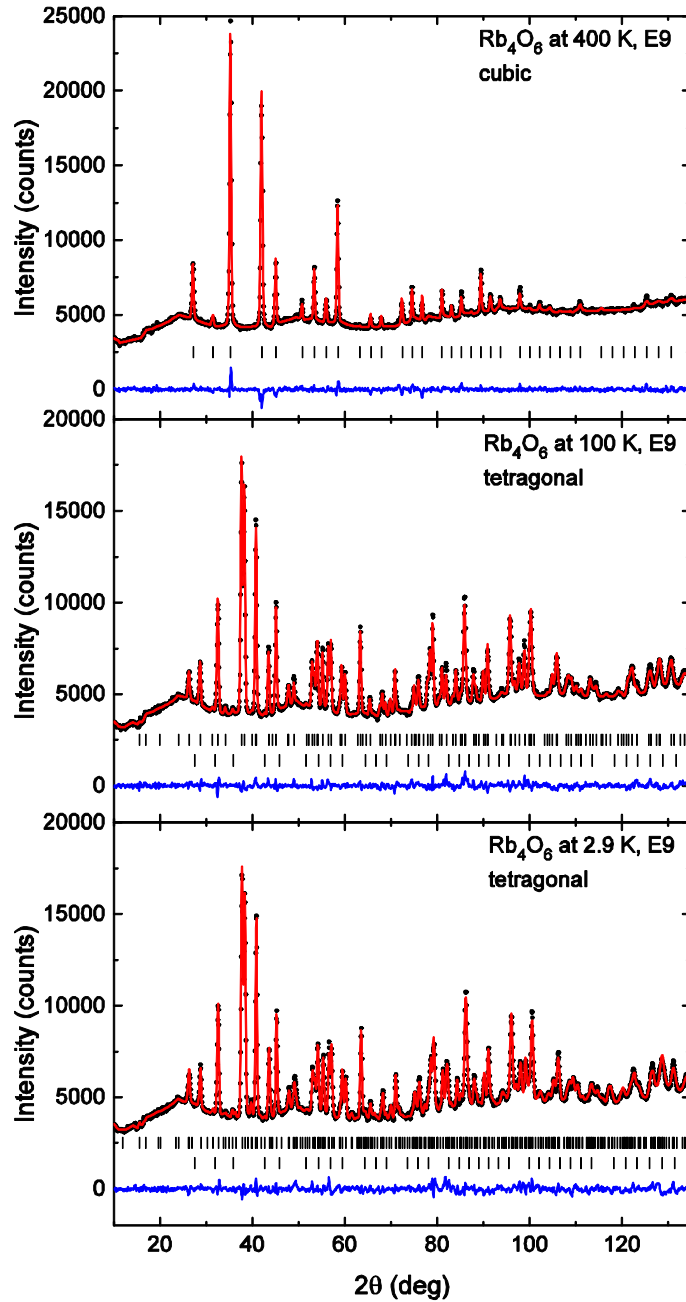


FIG. S2 Powder neutron diffraction patterns of Rb_4O_6 collected at instrument E9 ($\lambda = 1.7985 \text{ \AA}$). The pattern collected at 100 K was obtained after slow cooling which assured a nearly complete conversion to the tetragonal phase. At 2.9 K additional Bragg reflections were found obeying the extinction rule $h + k + l = 2n + 1$. The calculated pattern (red solid line) is compared with the observations (black-filled circles). The positions of the nuclear reflections (black bars) of the cubic and tetragonal phase, as well as the difference pattern ($I_{\text{obs}} - I_{\text{cal}}$) (blue solid line) is shown.

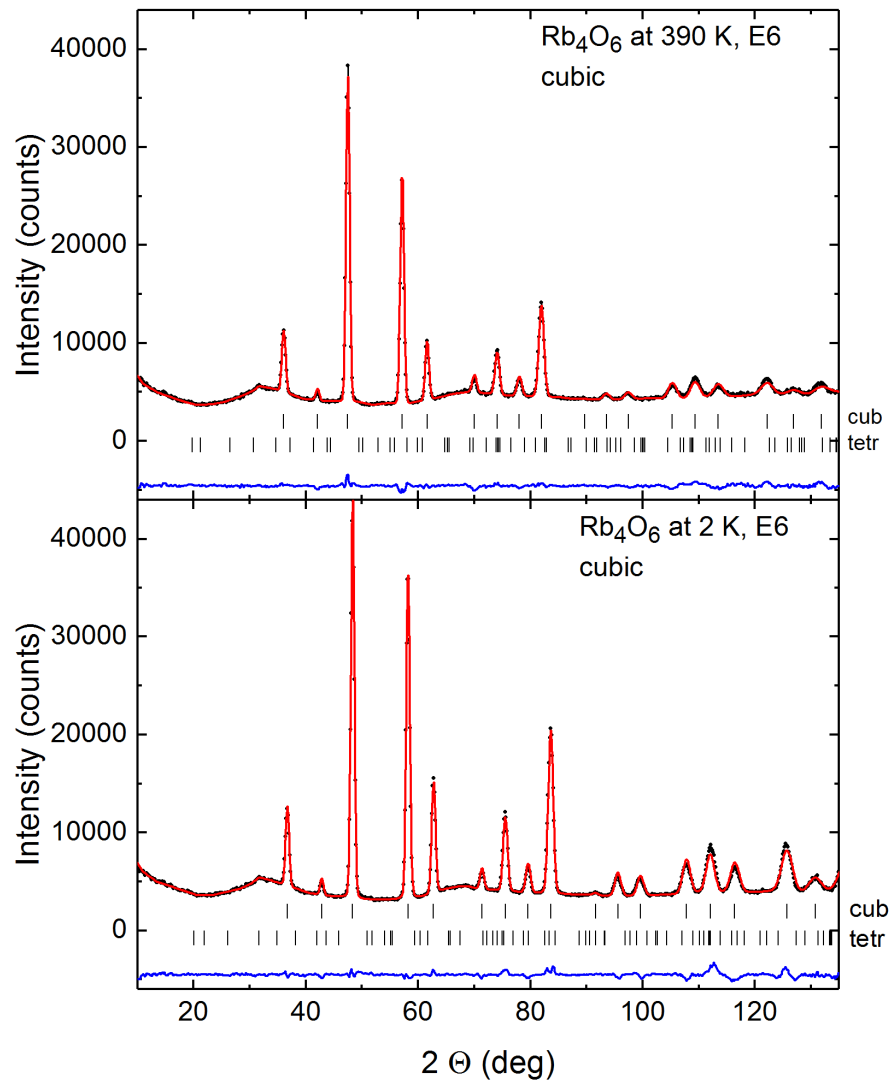


FIG. S3 Powder neutron diffraction patterns of Rb₄O₆ collected at instrument E6 ($\lambda = 2.426 \text{ \AA}$). The pattern collected at 2 K was obtained after quenching into liquid nitrogen, which completely preserved the cubic phase. The calculated pattern (red solid line) is compared with the observations (black-filled circles). The positions of the nuclear reflections (black bars) of the cubic and tetragonal phase, as well as the difference pattern ($I_{\text{obs}} - I_{\text{cal}}$) (blue solid line) is shown.

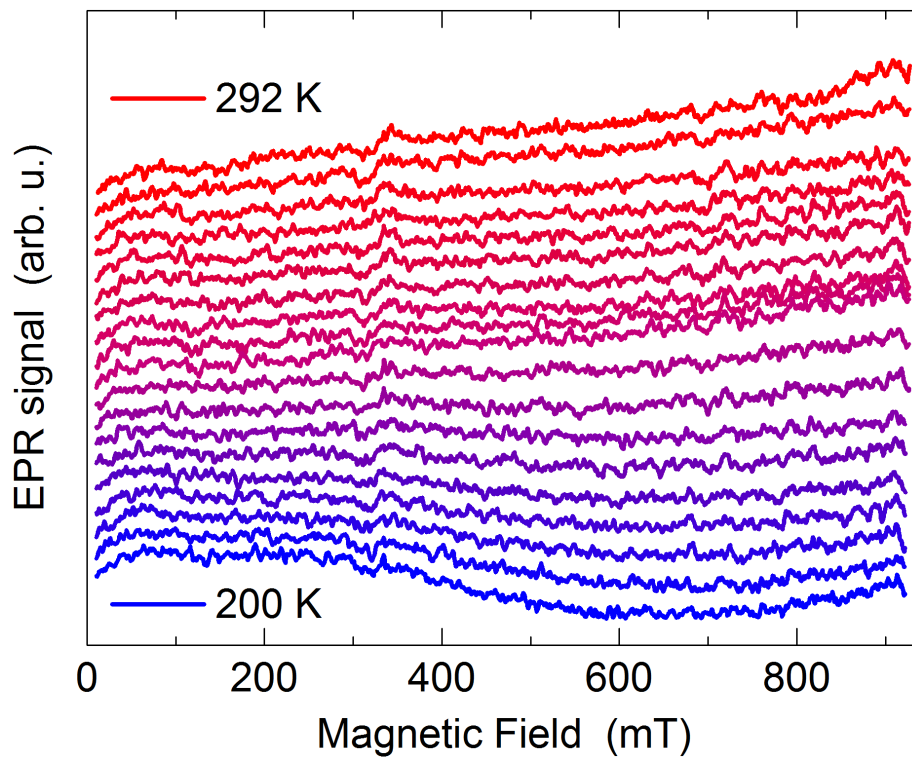


FIG. S4 The structural transition from the cubic (red) to the tetragonal (blue) phase as seen by the emergence of the EPR signal. The spectra were measured in 5 K steps.

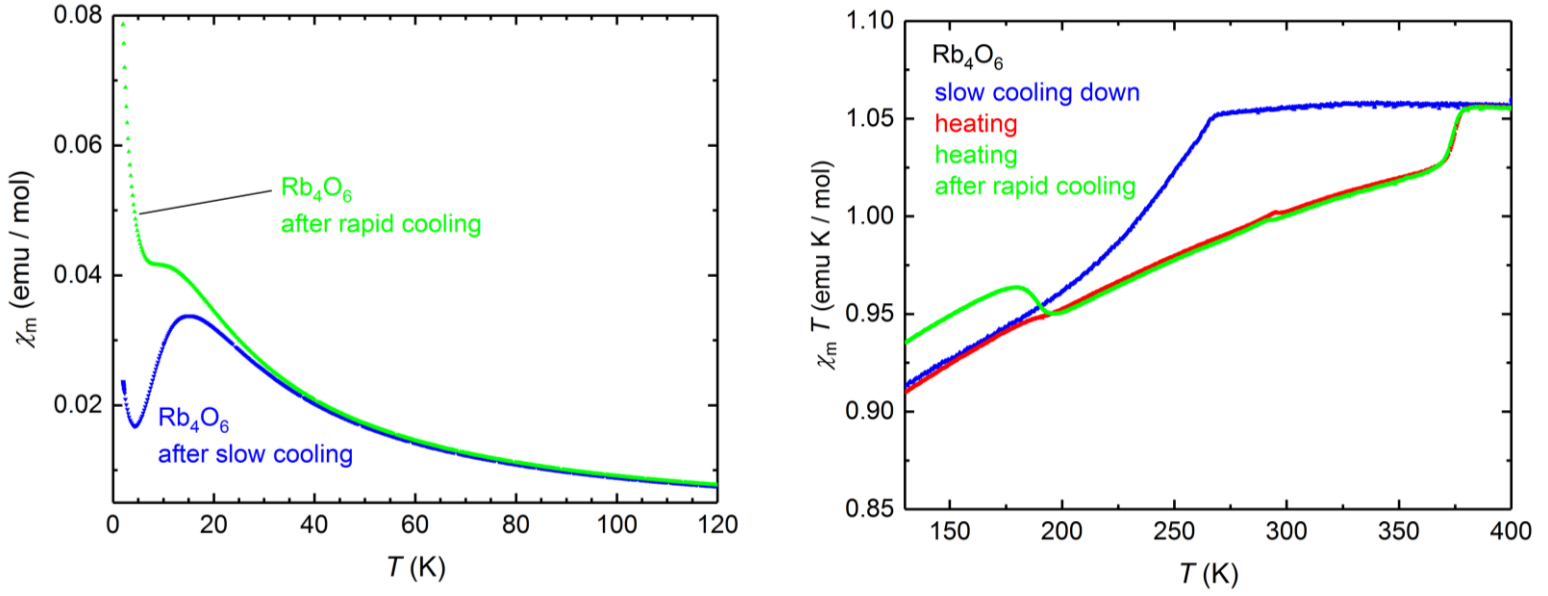


FIG. S5 Measurements of molar susceptibility, $\chi_m(T)$, of Rb₄O₆ powder using different cooling protocols. In the slow cooling experiment a cooling rate of 2 K/min was applied starting from 400 K, in the rapid cooling procedure a cooling rate of 20 K/min was applied. Left panel: Rapid cooling leads to an enhanced increased Curie tail in $\chi_m(T)$ at low temperatures which partly obscures the maximum associated with the tetragonal phase. This is a signature of an increased fraction of frozen-in cubic phase. Right: The frozen cubic phase is the origin for an anomaly near 180 K which reflects the transformation of the metastable cubic phase to the tetragonal phase. The reverse tetragonal to cubic transformation occurs near 370 K in both temperature protocols.

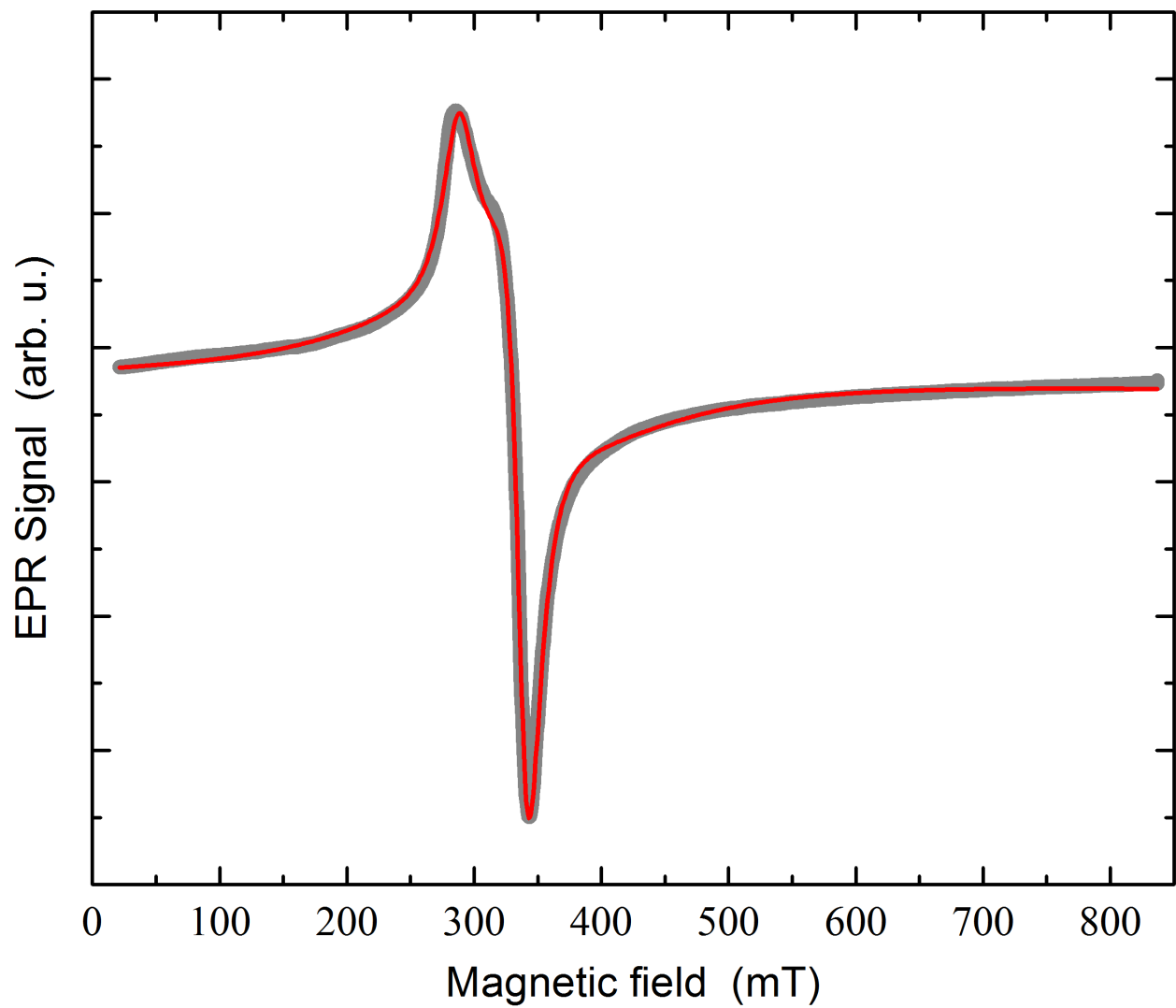


FIG. S6 The residual X-band EPR spectrum measured at 3.5 K in the tetragonal phase (gray line). Red line is a fit to Lorentzian lineshape with added g -factor anisotropy, yielding $g_x = g_y = 1.9757$, $g_z = 2.3110$, $\Delta B_x = \Delta B_y = 29.2$ mT and $\Delta B_z = 33.3$ mT.

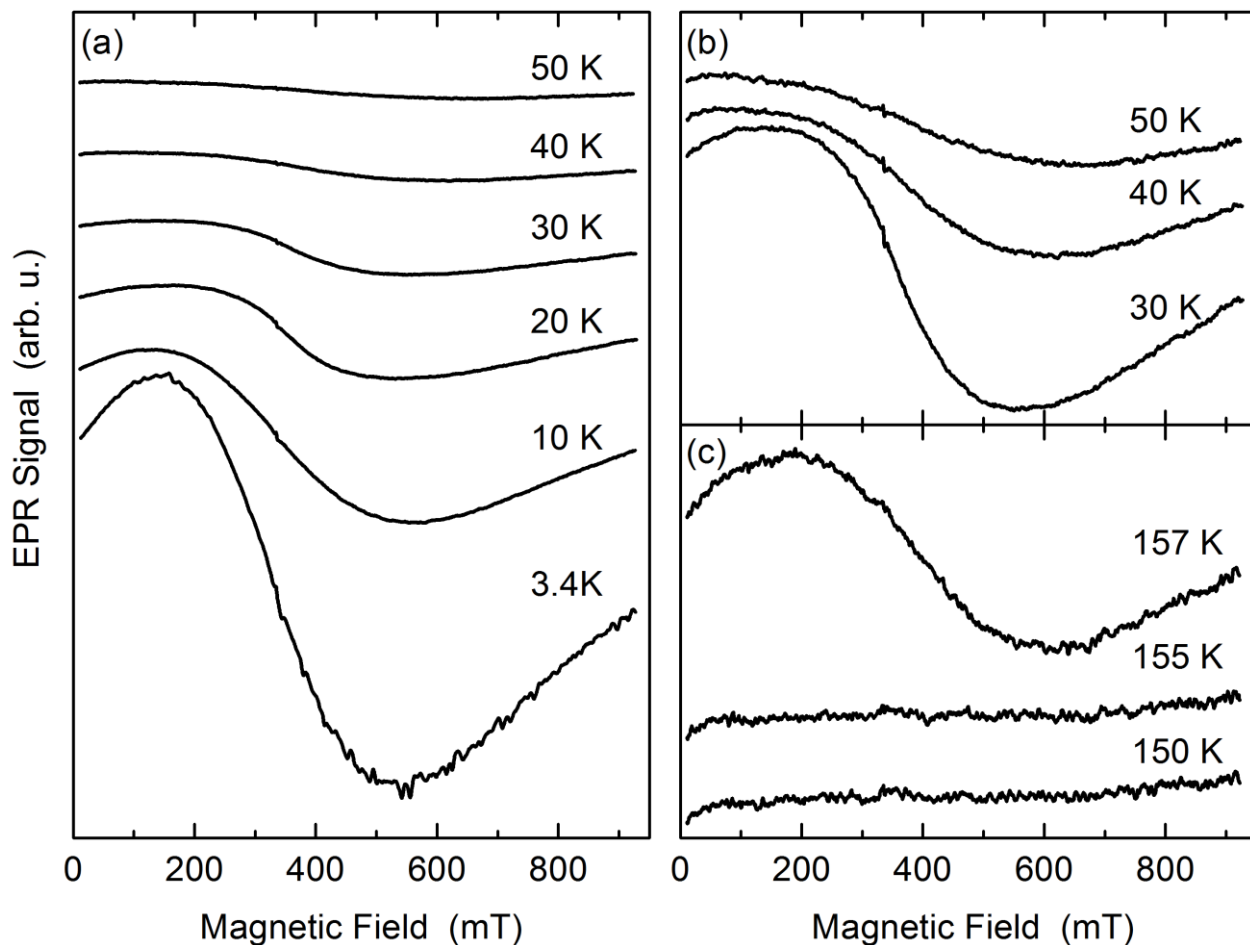


FIG. S7 The X-band EPR spectra of the cubic phase in the quench experiment. (a) Temperature dependence of the EPR spectra after quenching the sample from 400 K at selected temperatures between 3.4 K and 50 K. The spectra have a large linewidth, which even increases with increasing temperature. The EPR signal intensity, on the other hand, decreases with increasing temperature. (b) Comparison of X-band EPR spectra collected at 30, 40 and 50 K show large spectral broadening. (c) X-band EPR spectra at higher temperatures, showing the reappearance of the EPR signal characteristic of the tetragonal phase. According to EPR, the tetragonal phase thus starts to grow from the quenched cubic phase above 157 K, which is in excellent agreement with the powder neutron diffraction results (Fig. 2(b), main text).

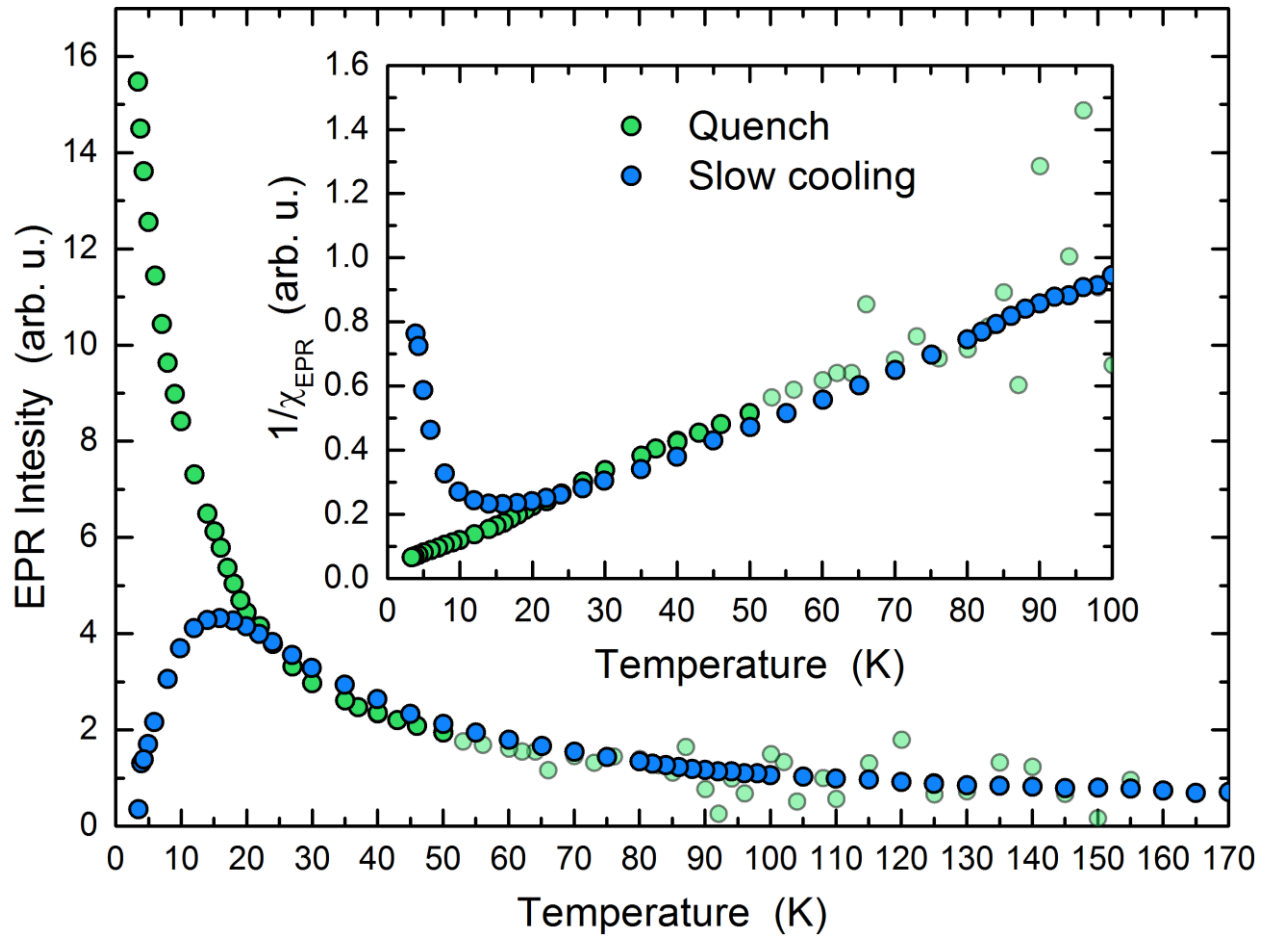


FIG. S8 The X-band EPR signal intensity of cubic (green circles) and tetragonal (blue circles) phase. Also, the green and blue circles represent EPR measurements when quenching and slow-cooling of the sample were used, respectively. The inverse EPR signal intensity demonstrates the Curie-Weiss temperature dependence of the EPR signal intensity, which in the case of cubic phase persists down to 3.4 K.

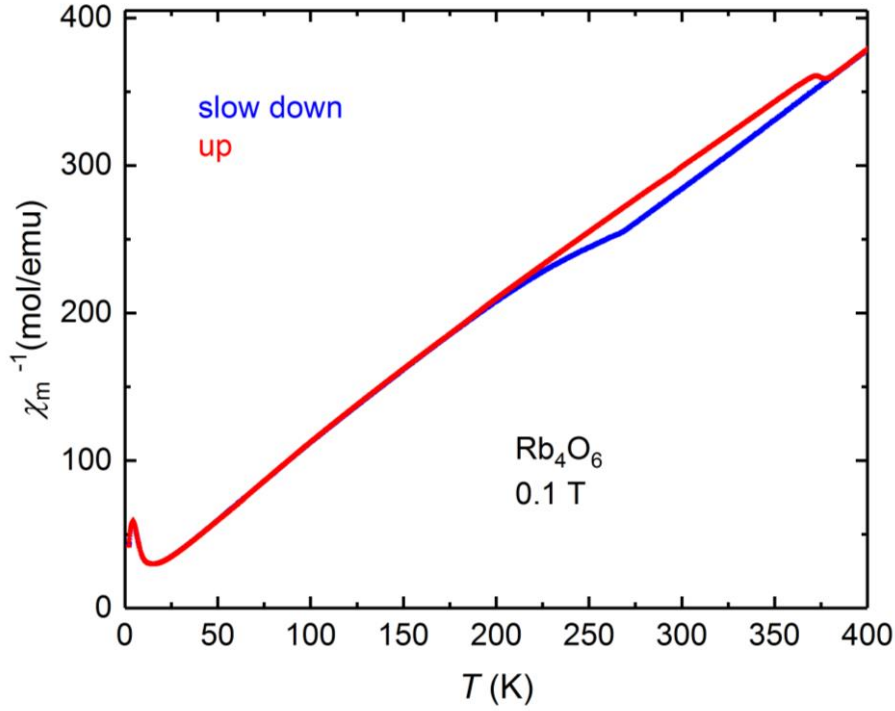


FIG. S9 Curie-Weiss plot of the magnetic susceptibility data of Rb_4O_6 measured at 1 T after slow cooling to 2 K. The anomalies reflect the cubic – tetragonal – cubic structural transitions on cooling and subsequent heating. Using the temperature range 50 to 120 K one obtains the effective magnetic moment $\mu_{\text{eff}} = 1.95 \mu_{\text{B}}$ and a Curie-Weiss temperature $\Theta = -7$ K for the tetragonal phase. For the cubic phase one obtains $\mu_{\text{eff}} = 2.05 \mu_{\text{B}}$ and $\Theta = +1$ K for the temperature range from 320 to 400 K using the data from the cooling down protocol.

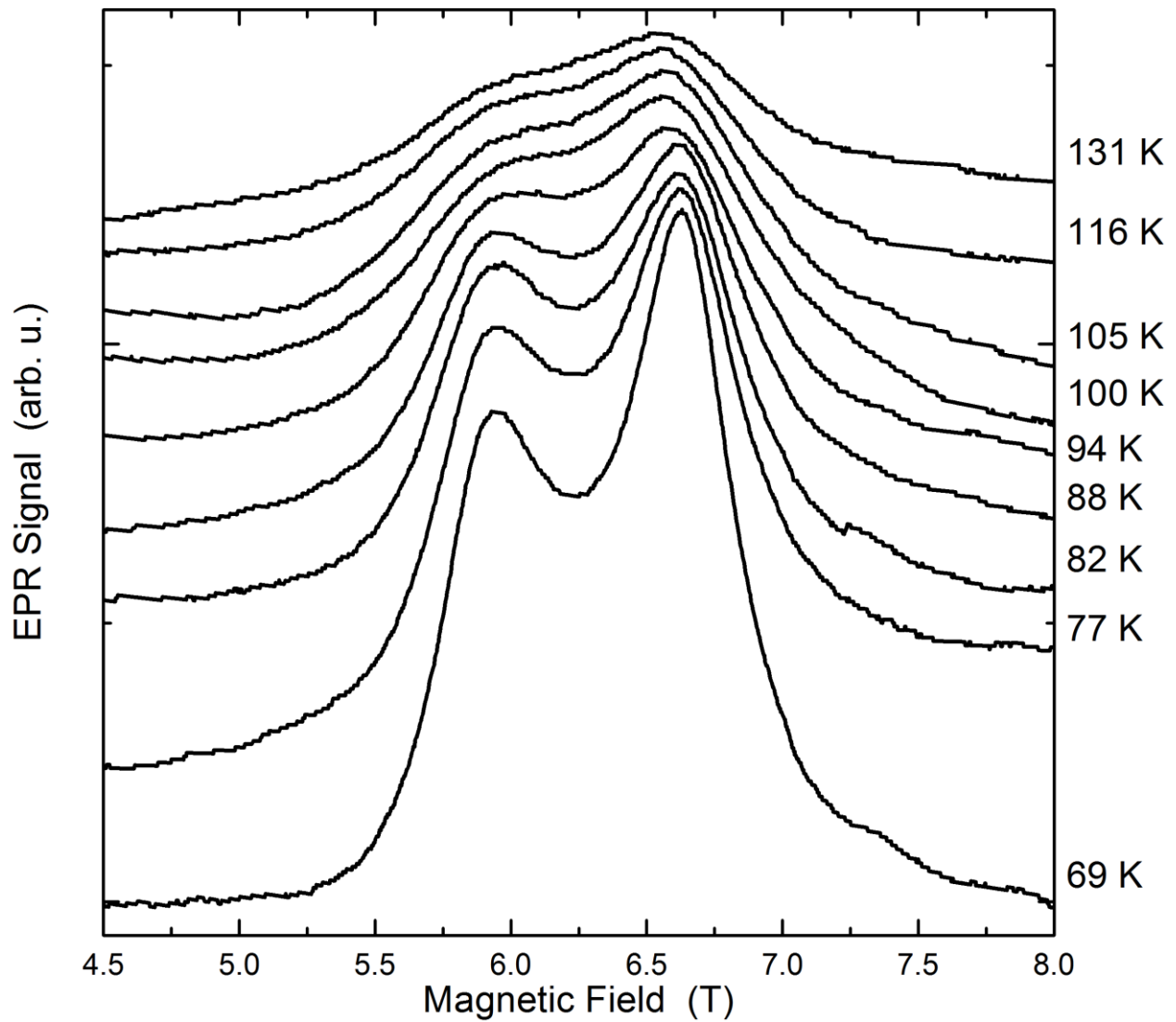


FIG. S10 Temperature dependence of the high-field EPR spectra measured at 186 GHz on heating. The splitting of the spectra is clearly visible and gradually becomes less pronounced above T_S .

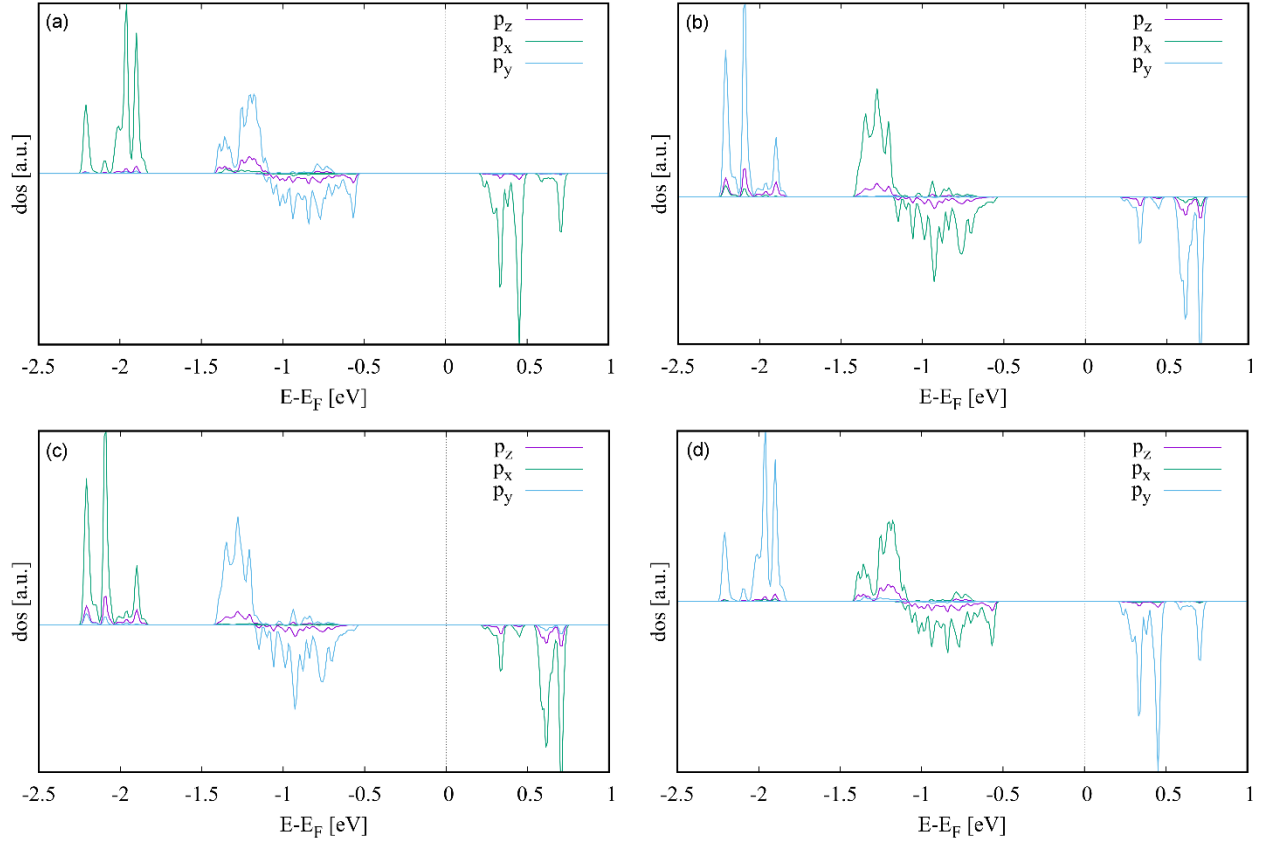


FIG. S11 Partial density of states (DOS) for selected O_2^- molecules, showing orbital ordering in the $P\bar{4}$ structure. (a) Partial DOS for O_2^- molecules labeled 8 and 9. (b) Partial DOS for O_2^- molecules 5 and 10. (c) Partial DOS for O_2^- molecules 6 and 11. (d) Partial DOS for O_2^- molecules 7 and 12. Atomic labels according to Fig. 1 (c) – (f) in the main text.

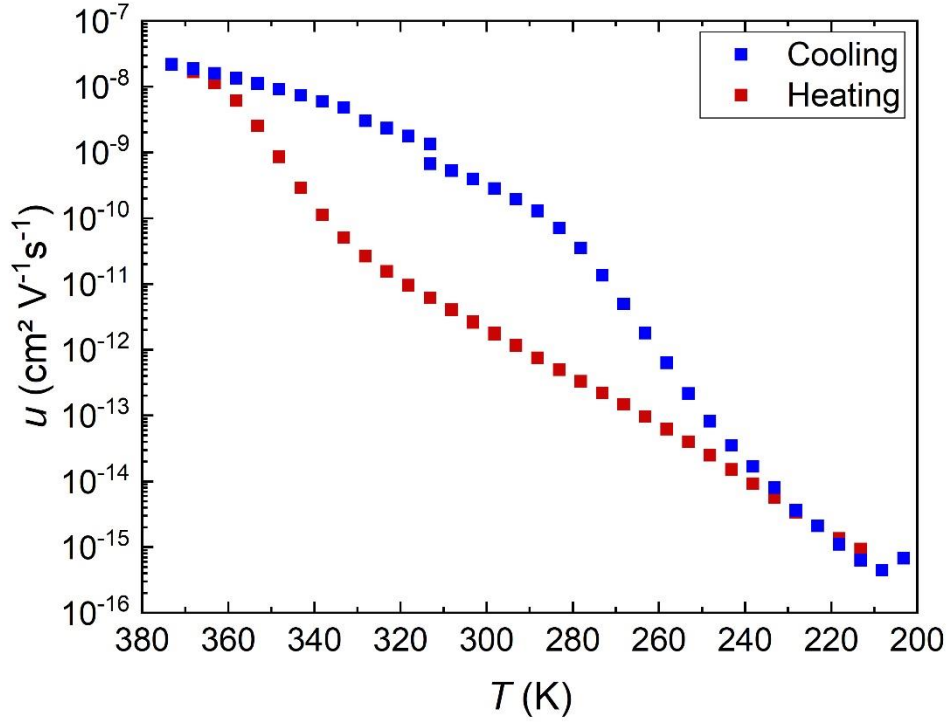


FIG. S12 Temperature-dependent charge carrier mobility of Rb_4O_6 . One assumption has been made: The cell volume shows a temperature-dependent expansion or contraction as shown in Fig. 2 of the main text. In the range of the phase transition a linear change of the volume from V_{cub} to V_{tet} and vice versa is assumed.

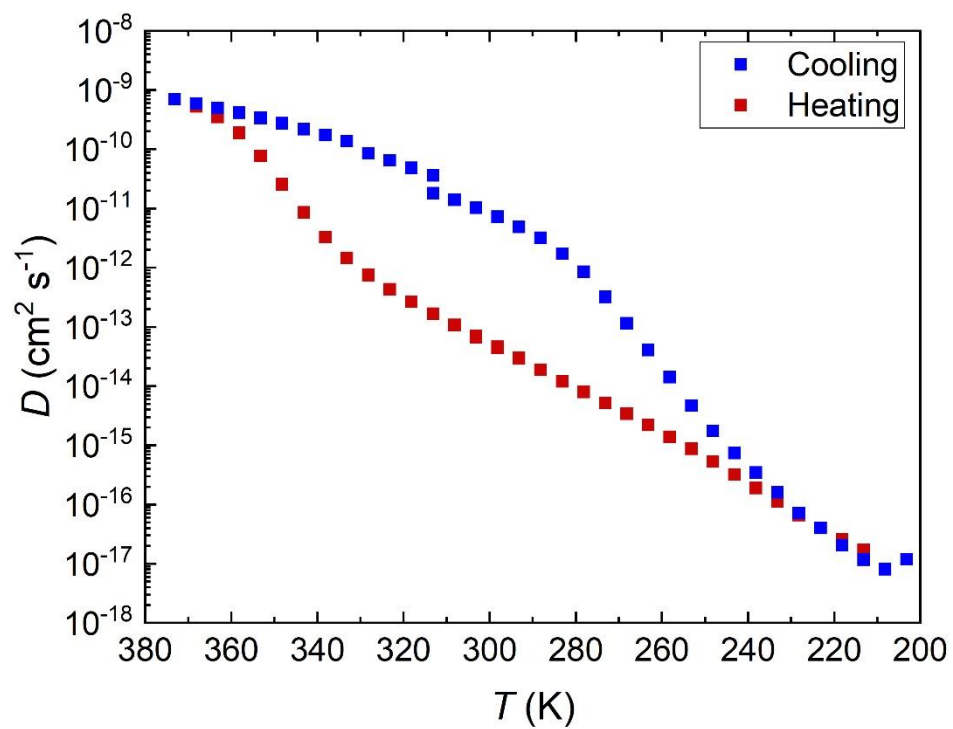


FIG. S13 Temperature-dependent diffusion coefficients of Rb_4O_6 . The diffusion coefficient of the electrons in the cubic phase is almost three orders of magnitude higher than the diffusion coefficient of the electrons in the tetragonal phase at the same temperature.

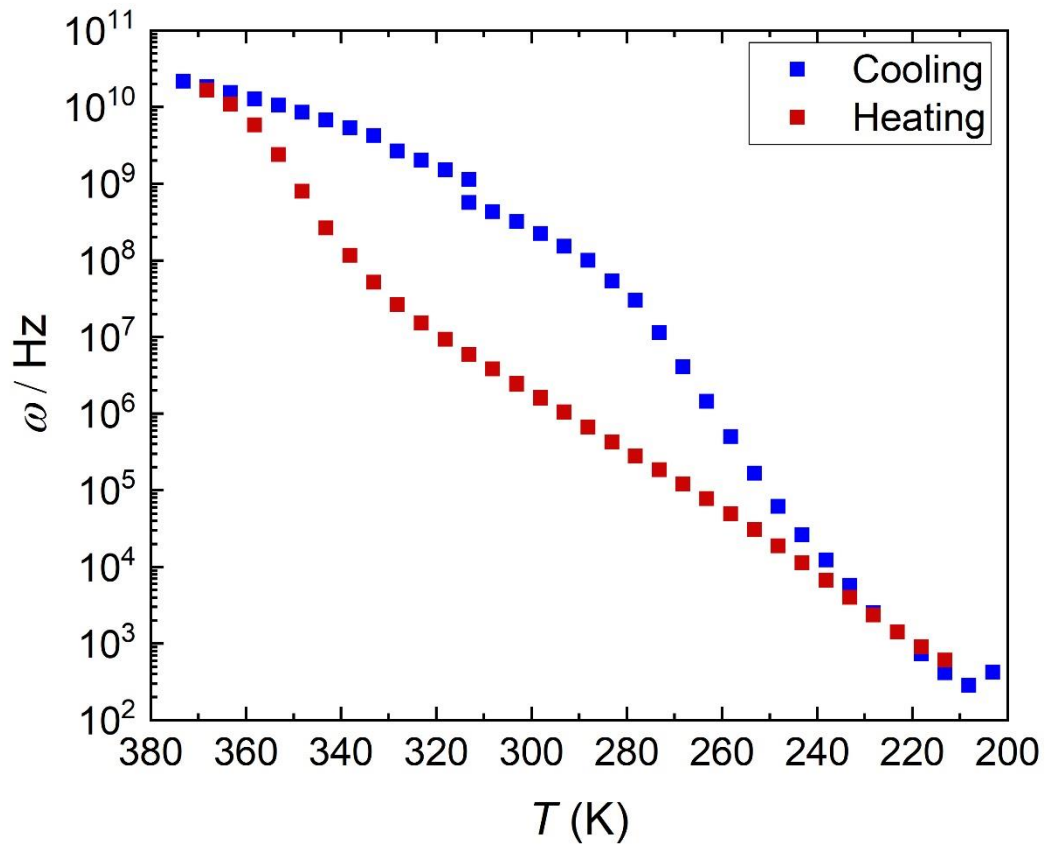


FIG. S14 Temperature-dependent jump frequency of the electrons in Rb_4O_6 . Jump distance (distance between the oxygen dumbbells) in the cubic phase: $a = 439$ pm. Jump distance in the tetragonal phase: $a = 418$ pm.

Table S1. Results of the crystal structure refinements of Rb_4O_6 from powder neutron diffraction data measured at instrument E9. The refinement of the cubic crystal structure was carried out in the space group $I\bar{4}3d$ (No. 220), while the two tetragonal structures were refined in $I\bar{4}$ (No. 82) and $P\bar{4}$ (No. 81), respectively. The isotropic temperature factors of the Rb atoms as well as those of the O atoms were constrained to be equal for the tetragonal phase.

Neutron data of Rb_4O_6 at 2.9 K					
Atom	Site	x	y	z	B [\AA]
Rb11	4h	0.6985(13)	0.9399(12)	0.0349(10)	0.57(5)
Rb12	4h	0.1944(12)	0.4539(13)	0.5533(9)	0.57
Rb21	4h	0.3196(11)	0.4545(12)	0.2018(10)	0.57
Rb22	4h	0.7947(11)	0.9259(10)	0.7176(9)	0.57
O11	2e	0	0	0.0738(3)	0.98(5)
O12	2f	$\frac{1}{2}$	$\frac{1}{2}$	0.5738(3)	0.98
O21	2g	0	$\frac{1}{2}$	0.1752(5)	0.98
O22	2g	0	$\frac{1}{2}$	0.3227(5)	0.98
O31	4h	0.2196(8)	0.1758(10)	0.4343(4)	0.98
O32	4h	0.7309(13)	0.6185(13)	0.9347(7)	0.98
O41	4h	0.2675(13)	0.1132(11)	0.3206(4)	0.98
O42	4h	0.7955(12)	0.5933(10)	0.8207(6)	0.98

$$a = b = 8.6494(3), c = 10.3473(5) \text{ \AA}, V = 774.10(7) \text{ \AA}^3, R_F = 0.041, \chi^2 = 3.36$$

Neutron data of Rb_2O_6 at 100 K					
Atom	Site	x	y	z	B [\AA]
Rb1	8g	0.6962(8)	0.9454(8)	0.0425(8)	1.55(4)
Rb2	8g	0.3093(9)	0.4471(9)	0.2067(8)	1.55
O1	4e	0	0	0.0735(3)	1.96(5)
O2	4f	0	$\frac{1}{2}$	0.1765(3)	1.96
O3	8g	0.2197(8)	0.1014(6)	0.4312(4)	1.96
O4	8g	0.2681(8)	0.1397(7)	0.3156(4)	1.96

$$a = b = 8.6700(3), c = 10.3641(4) \text{ \AA}, V = 779.06(6) \text{ \AA}^3, R_F = 0.043, \chi^2 = 2.86$$

Neutron data of Rb_2O_6 at 400 K					
Atom	Site	x	y	z	B [\AA]
Rb	16c	0.94437(18)	0.94437	0.94437	6.35(8)
O	24d	0.55304(27)	0	$\frac{3}{4}$	7.95(12)

$$a = b = c = 9.3861(5) \text{ \AA}, V = 826.92(15) \text{ \AA}^3, R_F = 0.106, \chi^2 = 3.72$$

Table S2. Interatomic distances (in Å) as obtained from the crystal structure refinements of Rb₄O₆ powder neutron diffraction data collected at instrument E9. Constraints were used to assure meaningful O-O distances for the superoxide O₂⁻ and peroxide O₂²⁻ units. Also listed are the tilting angles α and β (in °) of the superoxide O₂⁻ units relative to the *a* and *c* axes, respectively, obtained at 2.9 and 100 K.

Bond / Angle	Rb ₄ O ₆ at 2.9 K	Rb ₄ O ₆ at 100 K	Rb ₄ O ₆ at 400 K
	<i>P</i> $\bar{4}$ (No. 81)	<i>I</i> $\bar{4}$ (No. 82)	<i>I</i> $\bar{4}3d$ (No. 220)
<i>d</i> (Rb11-O11/O11)	2.689(11)/2.887(11)	2.695(7)/2.934(7)	2.999(3)
<i>d</i> (Rb12-O12/O12)	2.682(10)/2.979(10)	2.695/ 2.934	
<i>d</i> (Rb11-O21/O22)	2.819(11)/4.113(11)	2.876(8)/4.185(9)	2.916(2)
<i>d</i> (Rb12-O22/O21)	2.945(11)/4.277(11)	2.876/ 4.185	
<i>d</i> (Rb11-O32/O32/O32/O31)	2.947(16)/2.981(15)/3.299(16)/4.310(12)	3.030(10)/3.204(9)/3.250(9)/4.114(10)	
<i>d</i> (Rb12-O31/O31/O31/O32)	2.711(14)/2.832(15)/3.792(14)/4.048(12)	3.030/ 3.204/ 3.250/ 4.114	
<i>d</i> (Rb11-O42/O41/O42/O42)	2.881(14)/3.015(12)/3.188(14)/3.822(14)	2.928(10)/2.941(10)/3.598(9)/3.606(9)	
<i>d</i> (Rb12-O42/O41/O41/O41)	2.798(12)/2.903(15)/3.415(14)/ 3.844(14)	2.928/ 2.941/ 3.598/ 3.606	
<i>d</i> (Rb21-O12/O12)	2.825(11)/4.173(11)	2.851(9)/4.171(9)	
<i>d</i> (Rb22-O11/O11)	2.867(10)/4.141(11)	2.851/ 4.171	
<i>d</i> (Rb21-O21/O22)	2.806(10)/3.060(10)	2.739(8)/2.978(8)	
<i>d</i> (Rb22-O21/O22)	2.853(10)/2.662(9)	2.739/ 2.978	
<i>d</i> (Rb21-O32/O32/O32/O31)	2.828(15)/2.868(13)/3.354(15)/3.514(13)	2.868(10)/2.897(10)/3.248(10)/3.872(10)	
<i>d</i> (Rb22-O31/O31/O32/O31)	2.998(13)/3.063(11)/3.524(13)/3.862(13)	2.868/ 2.897/ 3.248/ 3.872	
<i>d</i> (Rb21-O42/O42/O41/O42)	3.053(15)/3.214(14)/3.243(14)/4.088(13)	2.828(10)/ 2.916(9)/3.426(10)/4.177(10)	
<i>d</i> (Rb22-O41/O42/O41/O41)	3.003(14)/3.069(13)/3.203(14)/4.147(11)	2.828/ 2.916/ 3.426/ 4.177	
<i>d</i> (O11-O11)	1.527(5)	1.524(4)	1.351(4)
<i>d</i> (O12-O12)	1.528(5)	1.524	1.351
<i>d</i> (O21-O22)	1.527(7)	1.525(4)	1.351
<i>d</i> (O31-O41)	1.336(10)	1.312(7)	1.351
α (O31-O41)	58.8(5)	38.3(5)	
β (O31-O41)	28.3(5)	20.1(5)	
<i>d</i> (O32-O42)	1.323(11)	1.312	1.351
α (O31-O41)	21.4(5)	38.3	
β (O31-O41)	26.9(5)	20.1	

Table S3. The connection between atomic labels (Fig. 6c in the main text and in the Tables S1, S2) and molecule labels (Figs. 1(c)-(f) in the main text) as used in DFT calculations for the crystal structure of Rb_4O_6 at 2.9 K ($P\bar{4}$).

Atomic labels	DFT molecule labels
O31 and O41	5, 6, 10 and 11
O32 and O42	7, 8, 9 and 12

Table S4. Hopping integrals t^2 between nearest neighboring O_2^- molecules as given by DFT calculations for the crystal structure of Rb_4O_6 at 100 K ($I\bar{4}$). Labels used are the same as in Figure 1 in the main text.

Molecule pair	t^2 [eV ²]	Molecule pair	t^2 [eV ²]	Molecule pair	t^2 [eV ²]
10 ↔ 5	0.378	8 ↔ 10	0.191	8 ↔ 12	0.018
7 ↔ 12	0.378	11 ↔ 7	0.191	11 ↔ 5	0.018
9 ↔ 10	0.225	8 ↔ 7	0.191	9 ↔ 5	0.014
6 ↔ 7	0.225	11 ↔ 10	0.191	6 ↔ 12	0.014
10 ↔ 6	0.225	8 ↔ 5	0.018	9 ↔ 12	0.014
9 ↔ 7	0.225	11 ↔ 12	0.018	5 ↔ 6	0.014

Table S5. Total energies for two different spin configurations as given by DFT calculations for the crystal structure of Rb_4O_6 at 2.9 K ($P\bar{4}$). Labels used are the same as in Figure 1 in the main text.

Molecule labels	5 8	9 10	7 11	6 12	Total energy [eV]
FM configuration	↑ ↑	↑ ↑	↑ ↑	↑ ↑	-65814.477743
AFM configuration	↑ ↓	↑ ↓	↑ ↓	↑ ↓	-65814.483039